

Two Computational Models for Simulating the Tumbling Motion of Elongated Particles in Fluids

Dominik Bartuschat^{a,*}, Ellen Fischermeier^b, Katarina Gustavsson^c, Ulrich Rüde^a

^a*Lehrstuhl für Systemsimulation, Friedrich-Alexander Universität Erlangen-Nürnberg, Cauerstrasse 11, 91058 Erlangen, Germany*

^b*Institut für Theoretische Physik I, FAU Erlangen-Nürnberg, Staudtstrasse 7, 91058 Erlangen, Germany*

^c*Department of Mathematics, Numerical Analysis/Linné Flow Centre, Royal Institute of Technology (KTH), 100 44 Stockholm, Sweden*

Abstract

Suspensions with fiber-like particles in the low Reynolds number regime are modeled by two different approaches that both use a Lagrangian representation of individual particles. The first method is the well-established formulation based on Stokes flow that is formulated as integral equations. It uses a slender body approximation for the fibers to represent the interaction between them directly without explicitly computing the flow field. The second is a new technique using the 3D lattice Boltzmann method on parallel supercomputers. Here the flow computation is coupled to a computational model of the dynamics of rigid bodies using fluid-structure interaction techniques. Both methods can be applied to simulate fibers in fluid flow. They are carefully validated and compared against each other, exposing systematically their strengths and weaknesses regarding their accuracy, the computational cost, and possible model extensions.

© 2015 Published by Elsevier Ltd.

Keywords: Fluid-particle interaction, Tumbling fibers, Slender body formulation, Lattice Boltzmann method

1. Introduction

Flows with suspended solid phase occur in many applications, and thus simulation techniques for such systems are receiving rapidly increasing interest. An important and mathematically interesting special case are fiber suspensions. In this article we will investigate two different computational models that represent the particulate solid phase in Lagrangian form. Particles will be treated as rigid, elongated three-dimensional geometric objects. Elongated is here understood as the situation that the shape of the particles has one dimension significantly larger than the others, and thus our two methods apply to suspensions with fibers or rods. For the fluid phase, we assume in this article creeping flows, i. e. the Reynolds number is small and the Stokes equation can provide a sufficiently accurate approximation to the flow field.

The first method is based on a boundary integral formulation for Stokes flow, and approximations exploiting the slenderness of the suspended particles. This approach leads to an explicit representation of the hydrodynamic interactions between particles that avoids computing the flow field explicitly [1]. The resulting global system representing the hydrodynamic interactions for this slender body formulation (SBF) must be solved at each time step during a simulation [2, 3].

The second method employs a full 3D Eulerian representation of the fluid using the lattice Boltzmann method (LBM), while the particles are represented as rigid, fully resolved, geometric objects that can move freely through the simulation domain. Here fluid-structure-interaction (FSI) mechanisms are used to couple the flow field to the dynamics of the suspended particles. This approach can lead to very high computational cost since the mesh for computing the flow field must be so fine that the geometry of the suspended objects is resolved accurately enough. Here using parallel supercomputers is often inevitable [4].

Among the many interesting effects in fiber suspensions

*Corresponding author

Email address: dominik.bartuschat@cs.fau.de (Dominik Bartuschat)

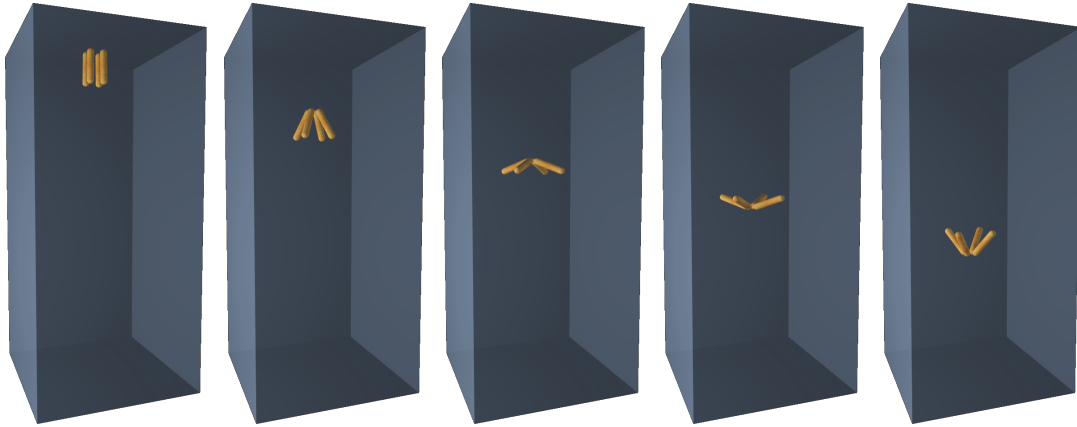


Figure 1. Tumbling motion of four spherocylinders sedimenting in Stokes flow, simulated with LBM.

we highlight here the tumbling trajectories of sedimenting fibers in Stokes flow, as visualized in the image sequence in Fig. 1. Experimental results for tumbling rods were presented in [5]. Qualitatively correct simulations of this dancing motion can be achieved both with the LBM and the SBF models. To the best of our knowledge, FSI-based simulations with the LBM that show this phenomenon have not been reported before.

We will find that the SBF can be more efficient and accurately represents the hydrodynamic interactions when the assumptions on which it is based are well-satisfied. The LBM, in contrast, can be used in more general settings and permits many extensions, such as simulating flows with higher Reynolds number and more general boundary conditions, and treating objects with different geometry than rigid fibers. The LBM based approach can finally also represent scenarios with particles colliding with each other or with the bounding walls. These possible future extensions justify to develop a method with higher computational cost.

Besides the development of the LBM with FSI techniques for fiber suspensions, the primary goal of this paper is the systematic comparison of the two different simulation approaches and to assess their strengths and weaknesses. This comparison will also be used for the cross-validation of the methods. For complicated multi-physics scenarios such as particles in suspension, the validation increasingly becomes a challenge in itself, especially when analytical model solutions are not known, and when only sparse data from physical experiments exist. In this case, the comparison of two different simulation methodologies can serve as a powerful alternative to assert the correctness of the models, the algorithms, and their implementation in software. In this paper, we study in particular the accuracy of the simulations by comparing the translational settling velocity and the angular velocity to analytical solutions for the slender body motion. As a more complex scenario with interacting particles, we will investigate tumbling fibers.

The simulation with four tumbling fibers in Fig. 1 illustrates the potential of the methodology for future applications that may involve many interacting particles.¹ This article, however, is restricted to the analysis and validation of the simpler case of two tumbling elongated particles.

The SBF [6, 2, 3] is an asymptotic method derived from the integral representation of Stokes equations and leads to a model consisting of a coupled system of one-dimensional integral equations. The model uses a discrete representation of each ellipsoidal fiber in terms of the fiber center line and takes into account the hydrodynamic interactions of the fluid and the fibers. Due to the long-range nature of the hydrodynamic interaction, a dense system of equations must be solved. This method is further described in Sec. 3. The SBF has successfully been used for numerical simulations of fiber suspension in gravity induced sedimentation, see e. g. [7, 8].

The LBM follows an alternative modeling paradigm that explicitly represents the flow field in an Eulerian way, as described by the Stokes or Navier-Stokes equations. A numerical simulation then requires the discretization on a grid, and the definition of interactions between particles and fluid and vice versa. Such approaches have been studied e. g. in [9, 10]. Suspended particles must then be mapped to the grid similarly to an immersed interface technique [11] or fictitious domain method [9].

In this article the LBM is employed as an alternative to a Navier-Stokes solver. The LBM uses a coupling between Eulerian fluid and Lagrangian particles via the momentum exchange method [12, 13, 14] and by imposing moving boundary conditions on the fluid. This approach allows the representation of arbitrary geometric shapes, provided the grid resolution of the LBM method permits a sufficiently accurate resolution. For simulations of ensembles of several particles with good resolution, this leads to very large grids with small mesh size. These in turn lead to

¹Animation available via permalink:
<https://www10.cs.fau.de/permalink/eehaugh300>

short time steps in the LBM algorithm. Combined, these effects can result in very large computational cost that can only be provided by parallel high performance computing. This article therefore essentially depends on using the massively parallel and efficient software frameworks WALBERLA [15] and *pe* [16, 17]. WALBERLA supports fluid-structure interaction with the LBM in a massively parallel setting [4, 18] by coupling it to the physics engine *pe* for rigid body dynamics. The elongated particles simulated in this paper are modeled as spherocylinders of fixed radius and with different aspect ratios.

A validation of spherocylinder simulations with the *pe* in absence of hydrodynamic interactions was presented in Fischermeier et al. [19]. The fluid-particle interaction algorithm with the coupled frameworks has been developed and validated for charged spherical particles in microfluid flows in [20].

The LBM was previously applied to study the sedimentation of elongated rigid particles at low to moderate Reynolds numbers. Xia et al. [21] simulated the settling of single elliptical particles in a narrow channel with a two-dimensional multi-block LBM method to examine the wall influence on flow patterns for different density, aspect, and blocking ratios. The settling of a single spherocylinder in a channel was studied with a two-dimensional lattice Boltzmann direct-forcing fictitious domain method in Nie et al. [22] for different solid-fluid density ratios. In [23], the settling of cylindrical fibers was investigated for different aspect ratios at moderate Reynolds numbers. The simulations were performed in three dimensions with the LB momentum-exchange method in a box moving with the particles.

The LB momentum-exchange method was previously applied to simulate the rotational motion of single elongated particles in shear flow. Ku and Lin [24] simulated the rotation of single rigid cylinder-shaped particles in planar Couette flow for moderate Reynolds numbers. The influence of the Reynolds number and the flow confinement was examined in two dimensions for a given aspect ratio. Mao and Alexeev [25] presented three-dimensional simulations of the motion of single spheroidal particles in an unbounded shear flow at low to moderate Reynolds numbers. In their work, the influence of fluid and particle inertia on the rotational motion was investigated for different aspect ratios and initial orientations.

The physical models for elongated particles in creeping flow are summarized in Sec. 2. Details about the SBF and LBM are introduced in Sec. 3 and Sec. 4, respectively. The simulation of a single elongated particle is validated in Sec. 5, and the tumbling motion of two sedimenting particles is studied in Sec. 6. Finally, the findings are summarized in Sec. 7 and possible model extensions are outlined.

2. Creeping flow with rod-like particles

2.1. Fluid dynamic equations

In this article we are concerned with the flow of small rigid particles suspended in a viscous incompressible fluid. The flow of the fluid can be described by the Navier-Stokes equations,

$$\rho_f \left[\frac{\partial \mathbf{u}}{\partial t} + \mathbf{u} \cdot \nabla \mathbf{u} \right] = -\nabla p + \mu_f \nabla^2 \mathbf{u} + \mathbf{f}_b, \quad (1)$$

$$\nabla \cdot \mathbf{u} = 0. \quad (2)$$

Here, \mathbf{u} and p denote the velocity and the pressure of the fluid, μ_f and ρ_f denote the dynamic viscosity and density of the fluid, and \mathbf{f}_b denotes the external body force density.

A density difference between the immersed particles and the surrounding fluid will give rise to a motion of the particles. For particles in incompressible fluids, the gravitational force acting on the fluid does not need to be considered explicitly. Instead, the effect of the resulting pressure gradient and of the gravitational force acting on the particle is accounted for in the force applied to the particle

$$\mathbf{F} = (\rho_p - \rho_f) \mathbf{g} V, \quad (3)$$

where ρ_p is the density of the particle, V denotes its volume, and \mathbf{g} is the gravitational acceleration.

The influence of the particle on the fluid will arise from the boundary condition the particle imposes on the fluid motion. For a rigid-body motion a no-slip condition is imposed meaning that the fluid velocity at the boundary of the particle is the same as the particle velocity. Boundary conditions must also be applied at the outer boundaries of the domain of interest. Which boundary conditions to use, depends on the flow case. In cases when only the motion of the particle is of interest, outer boundary conditions should be chosen that influence the flow field is as little as possible, e.g. periodic or free-slip boundary conditions (see Sec. 6.3 or Sec. 5.2).

2.2. Stokes equations

For small particles the velocity scale is usually small and therefore also the particle Reynolds number which is defined as

$$Re_p = \frac{UL}{\nu_f}. \quad (4)$$

Here the particle Reynolds number is based on a typical length, L , related to the size of the particle, as well as on a typical velocity U of the particle, and the kinematic viscosity of the fluid $\nu_f = \mu_f/\rho_f$. In this paper, we use the particle diameter $2r$ (see Fig. 2) as a typical length scale for the particle Reynolds number $Re_{p,d}$.

When $Re \ll 1$, the inertial and acceleration terms in the momentum equation (1) can be neglected, resulting in the Stokes equations

$$\nabla p - \mu_f \nabla^2 \mathbf{u} = \mathbf{f}_b, \quad (5)$$

$$\nabla \cdot \mathbf{u} = 0. \quad (6)$$

2.3. Single body motion at low Reynolds number

In some simple cases, e.g. one sedimenting sphere, cylinder or spheroid in an unbounded Stokes flow, analytical solutions can be found. These solutions are described below. More complex problems like interacting particles or particles in bounded fluid domains must be solved using computational models such as LBM or SBF.

In the regime of low Reynolds numbers, a linear relation exists between the force \mathbf{F} or the torque \mathbf{M} applied to a particle and the resulting translational velocity \mathbf{U} or angular velocity ω , respectively. For a slender body with rotational symmetry around its major axis, given by a unit vector \mathbf{t} , the corresponding equations are [26]

$$\mathbf{U} = \Xi^{-1} \mathbf{F} \quad \text{or} \quad \omega = \mathbf{M} / \gamma_r, \quad (7)$$

considering only torques applied perpendicular to \mathbf{t} . Here, γ_r is the rotational friction coefficient and Ξ the translational friction tensor. The latter depends on the translational friction coefficients γ_t^{\parallel} and γ_t^{\perp} for motion parallel and perpendicular to the symmetry axis \mathbf{t} of the particle as [26]

$$\Xi = \gamma_t^{\parallel} \mathbf{t} \mathbf{t}^T + \gamma_t^{\perp} (\mathbf{I} - \mathbf{t} \mathbf{t}^T), \quad (8)$$

with identity matrix \mathbf{I} and dyadic product $\mathbf{t} \mathbf{t}^T$. For forces applied parallel (lengthwise motion) or perpendicular (sidewise motion) to \mathbf{t} , the expression for \mathbf{U} in Eqn. (7) simplifies to

$$\mathbf{U}^{\parallel} = \mathbf{F} / \gamma_t^{\parallel} \quad \text{or} \quad \mathbf{U}^{\perp} = \mathbf{F} / \gamma_t^{\perp}, \quad (9)$$

respectively. Thus, the velocity and angular velocity of a particle under external forces and torques can be obtained provided the friction coefficients are known. However, these friction coefficients depend on the geometry of the particle and are known analytically only in a few cases described below.

Cox [27] derived analytical formulas for the force acting on a long, slender body at rest in Stokes flow from an expansion of the velocity field in terms of the parameter $\varepsilon = r/L$. Here, r is the radius of a particle and L its length (see Fig. 2). In case of a cylinder or spheroid, the translational motion can be described by the friction coefficients

$$\gamma_t^{\parallel} = 2 \frac{\pi \mu_f L}{\ln(1/\varepsilon) + C_1} \quad \text{and} \quad \gamma_t^{\perp} = 4 \frac{\pi \mu_f L}{\ln(1/\varepsilon) + C_2}, \quad (10)$$

where the constants C_1 and C_2 depend on the shape of the particles. For a circular cylinder $C_1 = -3/2 + \ln 2$ and

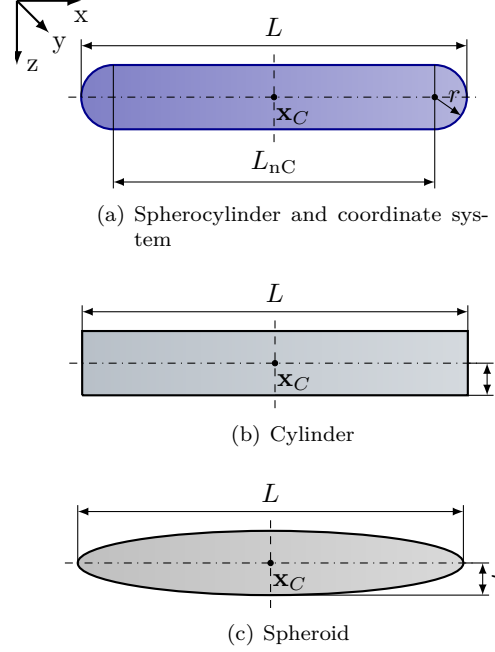


Figure 2. Slender body geometries and used coordinate system.

$C_2 = -1/2 + \ln 2$ holds, for a spheroid $C_1 = -1/2$ and $C_2 = +1/2$. The above formulas by Cox are valid for large aspect ratios, due to errors in the order of $O(\ln(\varepsilon)^{-3})$ [27].

In their work on diffusion of cylinders [28], Tirado et al. give the diffusion coefficients D for rotational diffusion, as well as diffusion parallel and perpendicular to the cylinder axis. These diffusion coefficients are at given temperature T linked to the friction coefficients γ via the Einstein-Smoluchowski relation $\gamma = k_B T / D$ with k_B as Boltzmann's constant. Using this relation, the analytical derivation in [28] leads to the translational frictional coefficients for lengthwise and sidewise motion, respectively

$$\gamma_t^{\parallel} = 2 \frac{\pi \mu_f L}{\ln a + v^{\parallel}} \quad \text{and} \quad \gamma_t^{\perp} = 4 \frac{\pi \mu_f L}{\ln a + v^{\perp}}, \quad (11)$$

with $a = \frac{L}{2r} = \frac{1}{2\varepsilon}$. For rotational motion perpendicular to the cylinder axis, according to Tirado it holds that

$$\gamma_r = \frac{1}{3} \frac{\pi \mu_f L^3}{\ln a + \delta^{\perp}}. \quad (12)$$

The results of Tirado et al. closely resemble those of Cox, however, the shape-dependent corrections v and δ are functions of a . In [28], Tirado et al. presented the following relations as simple quadratic fits in $\frac{1}{a}$ to the numerical values obtained in previous work [29, 30]

$$v^{\parallel} = -0.207 + 0.980/a - 0.133/a^2, \quad (13)$$

$$v^{\perp} = 0.839 + 0.185/a + 0.233/a^2, \quad (14)$$

$$\delta^{\perp} = -0.662 + 0.917/a - 0.050/a^2. \quad (15)$$

With these corrections, the Tirado results are valid for aspect ratios in the range of $4 < 1/\varepsilon < 60$ [28].

For the friction coefficients of the spherocylinders used as model particles in our LBM simulation, no analytical formulas are known. However, the above relations for cylinders give a good approximation for what to expect in case of spherocylinders (see Sec. 5). In this article, we will use the more recent results of Tirado et al. as reference.

3. The slender body formulation

Stokes equations can be reformulated in terms of a boundary integral equation. In this framework the fluid velocity due to the motion of a single particle can be computed by solving an integral equation stated solely over the particle surface.

Consider a straight, rigid and slender particle of length L and radius r . If the particle has a large aspect ratio, *i.e.* $L \gg r$, it can be referred to as a *slender body*. For slender bodies, a slender body approximation can be used.

3.1. Non-local slender body approximation

The slender body approximation is an asymptotic model derived from an integral representation of Stokes equations. The model relates the velocity of the slender body's surface to forces that are consistent with that motion and are exerted along its *centerline*. In the derivation, higher-order terms in the slenderness parameter $\varepsilon = r/L$ have been neglected and the accuracy of the final equation for the velocity of the fiber center-line is of order $O(\varepsilon^2 \ln \varepsilon)$. For several interacting fibers, the accuracy is of $O(\varepsilon)$. For details on the derivation, see the work of Batchelor [6], Keller and Rubinow [31], Johnson [2], and Götz [32].

3.1.1. Fiber velocities and force distribution

Assume that we have a system of M fibers. Let the center-line of each fiber be parameterized by $s \in [-l, l]$ where l is the half length of the fiber. For fiber \mathbf{m} the coordinates of the center-line is given by $\mathbf{x}_\mathbf{m}(t) = \mathbf{x}_\mathbf{m}(t) + s\mathbf{t}_\mathbf{m}(t)$ where $\mathbf{x}_\mathbf{m}$ is the center point and $\mathbf{t}_\mathbf{m}$ the unit tangent vector of the fiber and $\mathbf{m} = 1, 2, \dots, M$.

Assuming that the fluid exerts a force per unit length $\mathbf{f}_\mathbf{m}$ on fiber \mathbf{m} , the slender body approximation for the velocity of the center-line of fiber \mathbf{m} is given by

$$8\pi\mu_f(\dot{\mathbf{x}}_\mathbf{m} + s\dot{\mathbf{t}}_\mathbf{m}) = [d(\mathbf{I} + \mathbf{t}_\mathbf{m}\mathbf{t}_\mathbf{m}^T) + 2(\mathbf{I} - \mathbf{t}_\mathbf{m}\mathbf{t}_\mathbf{m}^T)]\mathbf{f}_\mathbf{m}(s) + (\mathbf{I} + \mathbf{t}_\mathbf{m}\mathbf{t}_\mathbf{m}^T)\bar{\mathbf{K}}[\mathbf{f}_\mathbf{m}](s) + \mathbf{V}_\mathbf{m}(s). \quad (16)$$

Here d is a geometry parameter

$$d = -\ln(\varepsilon^2 e), \quad (17)$$

and $\bar{\mathbf{K}}[\mathbf{f}](s)$ is an integral operator given by

$$\bar{\mathbf{K}}[\mathbf{f}](s) = \int_{-l}^l \frac{\mathbf{f}(s') - \mathbf{f}(s)}{|s' - s|} ds'. \quad (18)$$

The contribution to the velocity of fiber \mathbf{m} from the hydrodynamic interaction of all other fibers in the system is accounted for in $\mathbf{V}_\mathbf{m}(s)$ as

$$\mathbf{V}_\mathbf{m}(s) = \sum_{l=1}^M \int_{-l}^l \mathbf{G}(\mathbf{R}_{l\mathbf{m}}(s, s')) \mathbf{f}_l(s') ds'. \quad (19)$$

where $\mathbf{R}_{l\mathbf{m}}(s, s') = \mathbf{x}_\mathbf{m} + s\mathbf{t}_\mathbf{m} - (\mathbf{x}_l + s'\mathbf{t}_l)$ is the distance between one point on fiber \mathbf{m} and one point on fiber l .

In free-space (no outer boundary conditions) the Green's function reads

$$\mathbf{G}(\mathbf{R}) = \begin{cases} \mathbf{S}(\mathbf{R}) + \frac{r^2}{2}\mathbf{D}(\mathbf{R}) & \text{if } l \neq m \\ \mathbf{0}, & \text{if } l = m. \end{cases} \quad (20)$$

Here, $\mathbf{S}(\mathbf{R}) = (\mathbf{I} + \hat{\mathbf{R}}\hat{\mathbf{R}}^T)/|\mathbf{R}|$ with $\hat{\mathbf{R}} = \mathbf{R}/|\mathbf{R}|$ is the free space Stokeslet and $\mathbf{D}(\mathbf{R}) = (\mathbf{I} - 3\hat{\mathbf{R}}\hat{\mathbf{R}}^T)/|\mathbf{R}|^3$ is the dipole doublet.

The unknowns in Eqn. (16) are the translational and the rotational velocities, $\dot{\mathbf{x}}_\mathbf{m}$ and $\dot{\mathbf{t}}_\mathbf{m}$, and the force distribution along the fiber $\mathbf{f}_\mathbf{m}(s)$. To close the formulation (16), we use the additional conditions stating that the integrated force and torque on each fiber must balance the external forces and torques applied to the fibers

$$\mathbf{F} = \int_{-l}^l \mathbf{f}_\mathbf{m}(s) ds, \quad \mathbf{M} = \int_{-l}^l s(\mathbf{t}_\mathbf{m} \times \mathbf{f}_\mathbf{m}(s)) ds. \quad (21)$$

To solve Eqns. (16) and (21), the force on each fiber is expanded as a sum of Legendre polynomials,

$$\mathbf{f}_\mathbf{m} = \frac{1}{2}\mathbf{F} + \sum_{n=1}^N \mathbf{a}_\mathbf{m}^n P_n(s), \quad (22)$$

where P_n is a Legendre polynomial of degree n and the coefficients $\mathbf{a}_\mathbf{m}^n$ are unknown vectors with three components, one for each direction in space. The choice of N will be a parameter in the numerical method. With this approach, the coefficients, $\mathbf{a}_\mathbf{m}^n$, will be given as the solution to a dense linear system of equations with $3MN$ unknowns. The system of equations is derived from Eqn. (16) using the force expansion Eqn. (22), orthogonality properties of Legendre polynomials, and the fact that the operator $\bar{\mathbf{K}}$ in Eqn. (18) diagonalizes under the Legendre polynomials, cf. [32]. For details on the derivation, see [3].

Once the system of equations for the Legendre coefficients has been solved, the force on each fiber can be computed, and the translational and rotational velocities for each fiber can be computed using

$$\dot{\mathbf{x}}_\mathbf{m} = \frac{1}{8\pi\mu_f L} [d(\mathbf{I} + \mathbf{t}_\mathbf{m}\mathbf{t}_\mathbf{m}^T) + 2(\mathbf{I} - \mathbf{t}_\mathbf{m}\mathbf{t}_\mathbf{m}^T)] \mathbf{F} + \frac{1}{8\pi\mu_f} \int_{-l}^l \mathbf{V}_\mathbf{m}(s) ds, \quad (23)$$

$$\dot{\mathbf{t}}_\mathbf{m} = \frac{3d}{2\pi\mu_f L^3} (\mathbf{M} \times \mathbf{t}_\mathbf{m}) + \frac{3}{2\pi\mu_f L^3} (\mathbf{I} - \mathbf{t}_\mathbf{m}\mathbf{t}_\mathbf{m}^T) \int_{-l}^l s \mathbf{V}_\mathbf{m}(s) ds. \quad (24)$$

By integrating Eqns. (23) and (24) in time, the position and orientations of the fibers can be updated.

3.1.2. Numerical algorithm

The numerical algorithm developed to solve this problem is presented in detail in [3] where also the accuracy of the numerical method is carefully studied. Here we will only give a short summary of the numerical algorithm.

In the numerical treatment of this problem, integrals of the form

$$\int_{-1}^1 \left[\int_{-1}^1 \mathbf{G}(\mathbf{R}(s, s')) P_k(s') ds' \right] P_n(s) ds \quad (25)$$

must be computed. Note that in order to use the Legendre expansion, the equations are solved in a dimensionless form such that $-1 \leq s \leq 1$. For the inner integral in Eqn. (25) formulas for analytic integration have been developed [3]. The outer integral in Eqn. (25) is evaluated numerically by splitting the integration interval into N_q sub intervals, using a three-point Gauss quadrature rule on each interval.

The linear system of equations for the coefficients in the Legendre expansion is a dense system and is solved iteratively using GMRES which on average converges (depending on the distance between the fibers) within four or five iterations.

To update the position of the fibers, Eqn. (23) and Eqn. (24) are discretized in time using an explicit second-order time-stepping scheme with a fixed time step.

3.1.3. Extension to periodic boundary conditions

To perform simulations in a periodic domain, we must work with a periodized version of the Green's function in Eqn. (19). This term will now also include the contribution from all periodic images of the fibers. It has no closed analytical form, but can be thought of as a sum over an infinite periodic array of free space Stokeslets.

The periodic Stokeslet is evaluated through sums in real and Fourier space, and although rapidly converging, it is more costly to evaluate than a Green's function with a closed analytical expression. Therefore, parts of the periodic Stokeslet is initially evaluated on a uniform grid with grid size h_g , covering the domain $[0, L_x/2] \times [0, L_y/2] \times [0, L_z/2]$. Due to symmetries, trilinear interpolation can be used to obtain the values needed for any coordinate in a periodic box of size $[-L_x/2, L_x/2] \times [-L_y/2, L_y/2] \times [-L_z/2, L_z/2]$.

For conditions on convergence of this sum and its practical evaluation, see [3].

The integral over the periodized Green's function is treated numerically in the same way as the outer integral in Eqn. (25).

4. Fluid-particle interaction with the lattice Boltzmann method

4.1. The lattice Boltzmann method

The lattice Boltzmann method (LBM) is a numerical scheme for simulating hydrodynamics based on kinetic theory of gases. In the LBM, the phase space is discretized into a Cartesian lattice $\Omega_{dx} \subset \mathbb{R}^D$ of dimension D with spacing dx , and a finite set of Q discrete velocities $\mathbf{c}_q \in \mathbb{R}^D, q \in \{1, \dots, Q\}$. Associated with each \mathbf{c}_q is a particle distribution function (PDF) $f_q : \Omega_{dx} \times T_{dt} \mapsto \mathbb{R}$ that represents the probability of an ensemble of molecules located at the lattice site $\mathbf{x}_i \in \Omega_{dx}$ to move at that velocity. These velocities are chosen such that within a time increment $dt = t_{n+1} - t_n$ with discrete time $T_{dt} = \{t_n : n = 0, 1, 2, \dots\} \subset \mathbb{R}_0^+$, PDFs can move to neighboring lattice sites, or rest at a site.

The generalized discrete lattice Boltzmann equation [33, 34] with collision matrix \mathbf{S}

$$f_q(\mathbf{x}_i + \mathbf{c}_q dt, t_n + dt) - f_q(\mathbf{x}_i, t_n) = \sum_j S_{qj} (f_j - f_j^{eq}) \quad (26)$$

is an approximation of the Boltzmann equation in discrete phase space that can be derived from a forward-difference discretization in time and a spatial upwind discretization [35, 36]. This equation describes the advection of PDFs between adjacent lattice sites and subsequent collisions that are represented by the collision operator in the right hand side. The equilibrium distribution function, f_q^{eq} , as proposed by He and Luo [37], is given by

$$f_q^{eq}(\rho_f, \mathbf{u}) = w_q \left[\rho_f + \rho_0 \left(\frac{1}{c_s^2} (\mathbf{c}_q^T \mathbf{u}) + \frac{1}{2c_s^4} (\mathbf{c}_q^T \mathbf{u})^2 - \frac{1}{2c_s^2} (\mathbf{u}^T \mathbf{u}) \right) \right] \quad (27)$$

and recovers the incompressible Navier-Stokes (momentum) equation up to an error of order $\mathcal{O}(\text{Ma}^3)$. Here, $\text{Ma} = \frac{U}{c_s}$ is the Mach number, a measure for compressibility that depends on the characteristic velocity U of the fluid and the thermodynamic speed of sound c_s of the lattice model. The equilibrium distribution function depends on the local fluid density $\rho_f(\mathbf{x}_i, t_n) = \rho_0 + \delta\rho(\mathbf{x}_i, t_n)$ with average value ρ_0 and fluctuation $\delta\rho$, and up to quadratic order on the local velocity \mathbf{u} . These macroscopic quantities can be computed as moments of f_q as

$$\begin{aligned} \rho_f(\mathbf{x}_i, t) &= \sum_q f_q(\mathbf{x}_i, t), \\ \mathbf{u}(\mathbf{x}_i, t) &= \frac{1}{\rho_0} \sum_q \mathbf{c}_q f_q(\mathbf{x}_i, t), \end{aligned} \quad (28)$$

and the pressure p is given by the equation of state for an ideal gas, $p(\mathbf{x}_i, t) = c_s^2 \rho_f(\mathbf{x}_i, t)$.

We use the D3Q19 model of [38] with $c = dx/dt$,

$$c_s = c/\sqrt{3} \quad (29)$$

and the following weights w_q for the different directions: $w_1 = 1/3$, $w_{2,\dots,7} = 1/18$, and $w_{8,\dots,19} = 1/36$.

We employ the stable and accurate two-relaxation-time (TRT) collision operator by Ginzburg [39, 40],

$$\sum_j \mathbf{S}_{qj} (f_j - f_j^{\text{eq}}) = \lambda_e (f_q^e - f_q^{\text{eq},e}) + \lambda_o (f_q^o - f_q^{\text{eq},o}). \quad (30)$$

with two relaxation parameters, $\lambda_e = -\tau^{-1}$ for even- and λ_o for odd-order non-conserved moments. Here, λ_o is a free parameter, and the dimensionless relaxation time τ (or collision frequency $\omega = \tau^{-1}$) is related to the kinematic viscosity of the fluid by

$$\nu = \left(\tau - \frac{1}{2} \right) c_s^2 \text{dt}. \quad (31)$$

With this definition, the LBM is second order accurate in space and time [35].

For the TRT operator, the PDFs are decomposed as $f_q = f_q^e + f_q^o$ into even and odd components

$$\begin{aligned} f_q^e &= \frac{1}{2}(f_q + f_{\bar{q}}) & \text{and} & & f_q^{\text{eq},e} &= \frac{1}{2}(f_q^{\text{eq}} + f_{\bar{q}}^{\text{eq}}), \\ f_q^o &= \frac{1}{2}(f_q - f_{\bar{q}}) & \text{and} & & f_q^{\text{eq},o} &= \frac{1}{2}(f_q^{\text{eq}} - f_{\bar{q}}^{\text{eq}}), \end{aligned} \quad (32)$$

with opposite velocities $\mathbf{c}_{\bar{q}} := -\mathbf{c}_q$. The local equilibrium distribution function for the incompressible LBM according to [37] is then given for each lattice site by

$$\begin{aligned} f_q^{\text{eq},e} &= w_q \left(\rho_f - \frac{\rho_0}{2c_s^2} (\mathbf{u}^T \mathbf{u}) + \frac{\rho_0}{2c_s^4} (\mathbf{c}_q^T \mathbf{u})^2 \right), \\ f_q^{\text{eq},o} &= w_q \frac{\rho_0}{c_s^2} (\mathbf{c}_q^T \mathbf{u}). \end{aligned} \quad (33)$$

In each time step $t_n \in T_{\text{dt}}$ the LBM performs a *collide step* and a *stream step*

$$\tilde{f}_q(\mathbf{x}_i, t_n) = f_q(\mathbf{x}_i, t_n) + \lambda_e [f_q^e(\mathbf{x}_i, t_n) - f_q^{\text{eq},e}(\mathbf{x}_i, t_n)] + \lambda_o [f_q^o(\mathbf{x}_i, t_n) - f_q^{\text{eq},o}(\mathbf{x}_i, t_n)] \quad (34)$$

$$f_q(\mathbf{x}_i + \mathbf{e}_q, t_n + \text{dt}) = \tilde{f}_q(\mathbf{x}_i, t_n), \quad (35)$$

where \tilde{f}_q denotes the post-collision state.

Boundary conditions are treated in the stream step by modifying the post-collision states of PDFs of fluid lattice sites \mathbf{x}_F next to a boundary. The adaption to the boundary condition is performed for the PDFs associated with directions \mathbf{e}_q , in which the neighboring cell at $\mathbf{x}_n = \mathbf{x}_F + \mathbf{e}_q$ lies on the boundary. For the simulations presented in this article, we apply no-slip and free-slip conditions at the domain boundary. These boundary conditions originate from lattice gas bounce-back conditions and specular reflection conditions, respectively [41]. Moreover, periodic boundary conditions are used that cyclically extend the domain in a dimension.

The no-slip boundary condition enforces zero velocity at the interface of two lattice cells by reverting the PDFs of the relevant directions as

$$f_{\bar{q}}(\mathbf{x}_F, t_n + \text{dt}) = \tilde{f}_q(\mathbf{x}_F, t_n). \quad (36)$$

For the BGK model, the effective wall locations depend on τ . The free TRT parameter λ_o allows to fix walls aligned with the lattice dimensions half-way between two lattice sites for $\lambda_o = -8(2 - \omega)/(8 - \omega)$ [42]. This parameter is used for all simulations performed in this article. The free-slip boundary condition enforces zero velocity in normal direction at the boundary, while retaining the tangential velocity components by reflecting the PDFs as

$$f_{\text{refl}(q)}(\mathbf{x}_F + \mathbf{e}_q - \mathbf{n}(\mathbf{n}^T \mathbf{e}_q), t_n + \text{dt}) = \tilde{f}_q(\mathbf{x}_F, t_n), \quad (37)$$

where \mathbf{n} denotes a normalized wall surface normal vector. The post-reflection direction associated with $f_{\text{refl}(q)}$ can be computed as $\mathbf{e}_{\text{refl}(q)} = \mathbf{e}_q - 2(\mathbf{n}^T \mathbf{e}_q)\mathbf{n}$.

Periodic boundary conditions are realized by streaming the PDFs of the relevant directions to fluid lattice sites located next to the boundary at the other side of the periodic domain.

In a domain with periodicity in all coordinate directions, and when a constant force is applied to the embedded particles at each time step (see Sec. 6), the system must be stabilized to prevent it from accelerating infinitely. To keep the net momentum in the system constant, we apply a *momentum stabilization technique*: The average velocity in the whole domain is computed and then subtracted from the macroscopic velocity when computing the equilibrium distribution function. Thus, the LBM performs relaxation towards a state with zero net momentum, while preserving all other properties.

4.2. The momentum exchange approach

The hydrodynamic interactions of the particles via the fluid with the LBM are modeled by means of the momentum exchange approach, as introduced by Ladd [12, 43]. This exploits the mesoscopic origin of the LBM to compute the momentum exchange between the fluid and the suspended particles directly from PDFs adjacent to the particle boundary. While the original method represents particles as fluid-filled shells, we use the more stable variant with solid particles according to Nguyen and Ladd [13].

The solid, rigid objects are mapped onto the lattice such that the lattice sites are divided into a set b of moving obstacle cells whose center is overlapped by particles and a disjoint set F of fluid cells. Thus, particles are represented as obstacle sites with a staircase approximation of their surface. The obstacle cells b that are adjacent to a fluid cell F in any direction q are denoted as surface cells s . The momentum transfer from particles to the fluid is modeled by the velocity bounce-back boundary condition [12]

$$\tilde{f}_q(\mathbf{x}_F, t_n + \text{dt}) = \tilde{f}_q(\mathbf{x}_F, t_n) - 2 \frac{\omega_q}{c_s^2} \rho_0 \mathbf{c}_q^T \mathbf{u}_s \quad (38)$$

that adapts the fluid velocity at a given fluid cell F adjacent to the moving boundary to the local velocity \mathbf{u}_s at

an obstacle surface cell s . The PDF that is bounced back from the obstacle is updated such that the usual no-slip boundary condition Eqn. (36) is recovered in the stationary case, i. e., when the fluid velocity matches the boundary velocity [12].

The amount of momentum $\delta \mathbf{p}_q$ transferred from the fluid to a particle within a time step along a given link in direction \mathbf{c}_q , can be computed (cf. [44]) as

$$\delta \mathbf{p}_q = [\mathbf{c}_q \tilde{f}_q(\mathbf{x}_F, t_n) - \mathbf{c}_{\bar{q}} \tilde{f}_{\bar{q}}(\mathbf{x}_F, t_n + dt)] d\mathbf{x}^3 \quad (39)$$

from the difference of the momentum densities associated with the incoming PDF of a fluid cell F , and the PDF reflected from the particle surface in direction $\mathbf{c}_{\bar{q}}$. The corresponding force acting on the particle along a given link can then be obtained from the relation $\mathbf{F} = \frac{d\mathbf{p}}{dt}$ and Eqn. (39) with $\tilde{f}_{\bar{q}}$ given by Eqn. (38). Summing up the force contributions of the momenta transferred from fluid cells F to neighbouring surface cells s of a given particle results in the overall hydrodynamic force on the particle as given in [13]

$$\mathbf{F}_h = \sum_s \sum_{q \in D_s} \left[2\tilde{f}_q(\mathbf{x}_F, t_n) - 2\frac{\omega_q}{c_s^2} \rho_0 \mathbf{c}_q^T \mathbf{u}_s \right] \mathbf{c}_q \frac{d\mathbf{x}^3}{dt}. \quad (40)$$

Here, $\mathbf{x}_F = \mathbf{x}_s + \mathbf{e}_{\bar{q}}$ and D_s is the set of direction indices q , in which a given s is accessed from adjacent F . The overall torque \mathbf{M}_h can be computed analogously to Eqn. (40) by replacing \mathbf{c}_q by $\mathbf{c}_q \times (\mathbf{x}_s - \mathbf{x}_C)$, with the particle's center of mass \mathbf{x}_C .

For simplicity, we use the mean density ρ_0 in Eqn. (38) and consequently Eqn. (40) instead of the fluid density ρ_f in the neighbouring fluid cell. This is a good approximation for incompressible LBM in absence of large pressure gradients. Moreover, as analysed in [13], even large deviations from ρ_0 would have negligible effect on the accuracy of the hydrodynamic force computation.

The solid particles lead to fluid cells appearing and disappearing due to particle movement. Lattice sites that are uncovered by a particle that is moving away are re-filled by setting the PDF at this site to the equilibrium distribution according to Eqn. (33). We use the mean density, together with the particle surface velocity at that cell from the previous time step to compute $f^{eq}(\rho_0, \mathbf{u}_s(\mathbf{x}_s(t_n - dt)))$.

4.3. Coupling the LBM to rigid body dynamics

For parallel fluid-particle interaction simulations, the previously described methods are implemented in the LBM-based flow solver WALBERLA that is coupled to the physics engine *pe*. Both software frameworks are designed for massively parallel simulations, using a domain partitioning approach for distributed memory parallelization with MPI. The coupling strategy and the implementation of the fluid-particle interaction algorithm are described in [45, 46] and are only outlined below.

WALBERLA [47, 15, 20] is a parallel software framework for simulating fluid flow that employs the LBM. For the distributed memory parallelization, the simulation domain is decomposed into a cartesian grid of equally sized blocks that are assigned to the different MPI processes. On each process, data from adjacent lattice sites on a neighboring process is accessible via ghost layers. WALBERLA performs in each time step the streaming (Eqn. (35)) and collision (Eqn. (34)) of the LBM that are fused to a performance-optimized stream-collide step. Incorporated in this step is the treatment of the boundary conditions applied at the domain boundary, together with the velocity bounce-back conditions (Eqn. (38)) at the particle surface that model the momentum transfer to the fluid based on the local particle velocities

The *pe* [16, 17] is a framework for large-scale parallel rigid multi-body dynamics simulations. The rigid objects are geometrically fully resolved, and their translational and rotational motion is computed including frictional collisions of individual particles. Of the algorithms for multi-contact problems available in the *pe*, we employ the parallel fast frictional dynamics (FFD) algorithm [16] that is based on Kaufman et al. [48]. For the parallelization, the domain is partitioned exactly as for WALBERLA. Each *pe* process handles the particles whose centers of mass are located in the associated subdomain. For the collision handling, each process additionally stores shadow copies of intersecting particles [49]. A detailed description of the parallel FFD's time-stepping procedure including MPI communication is provided in [45, 19].

The momentum transfer to the particles is modeled by computing the contributions to the hydrodynamic force at the particle surface in WALBERLA as Eqn. (40), from which the *pe* aggregates the total force acting on the center of mass and the corresponding torque. The new positions and orientations of the particles are computed in the subsequent *pe* step, together with their translational and angular velocities. These velocities affect the fluid motion in the next time step, which in turn influences the particles. This interaction modelling corresponds to a two-way coupling.

4.4. Parallel high performance computing for the LBM

The explicit time discretization of the LBM restricts the time increment, and thus often many time steps are required to simulate physically relevant phenomena. Due to its strictly local memory access pattern in the stream-collide step that involves only adjacent sites, the LBM allows for highly parallel simulations with excellent scalability. The parallel scalability of the fluid-particle interaction algorithm implemented in WALBERLA was presented in [4] on up to 294 912 parallel processes.

The LBM simulations for this article were performed on

the high performance clusters LiMa² of the computing center RRZE in Erlangen (Germany) and SuperMUC³ of the Leibniz Supercomputing Centre LRZ in Garching (Germany). LiMa comprises 500 compute nodes, each containing two Xeon 5650 ‘Westmere’ hexa-core processors running at 2.66 GHz and with 24 GB DDR3 RAM. SuperMUC comprises 18 thin islands with 512 compute nodes, each node containing two Xeon E5-2680 ‘Sandy Bridge-EP’ octa-core processors that are running at 2.5 GHz and that have 32 GB DDR3 RAM. The nodes of both parallel clusters are connected by a high-speed InfiniBand interconnect.

The technical data of the parallel LBM simulations on LiMa and SuperMUC for the single particle motion validation in Sec. 5 are summarized in Tab. 1. These simulations include validations of the translational and rotational motion, examinations of wall effects, and flow field visualizations. As overview, the minimal and maximal problem sizes and the associated parallel processes are shown, together with the minimal and maximal time step numbers and the runtimes.

Table 1. Parallel run data for single particle motion LBM simulations. Lists cluster, problem size ($L_x \times L_y \times L_z$), numbers of processes (#proc.) and time steps (#TS), and runtime (RT) for validations of translational (a) and rotational (b) motion, examining wall influence on translational (c) and rotational (d) motion, and flow field visualization (e).

	Cluster	$L_x \times L_y \times L_z$ [dx]	#proc.	#TS	RT [h]
a	Super-MUC	$2560^2 \times 2688$	$16 \times 16 \times 32$	37 000 88 800	8.0 19
b	LiMa	816^3	$8 \times 8 \times 12$	40 000 140 000	2.6 9.4
c	LiMa	$160^2 \times 1200$	$4 \times 4 \times 12$	61 540	0.9
		$640^2 \times 1200$	$8 \times 8 \times 12$		4.0
	Super-MUC	$832^2 \times 1200$			6.1
		$1920^2 \times 2240$	$16 \times 16 \times 32$	86 156	8.5
		$2560^2 \times 2688$		70 400	15
d	LiMa	168^3	$2 \times 3 \times 4$	80 000	1.3
		1296^3	$8 \times 8 \times 12$	84 000	19
e	LiMa	$832^2 \times 1200$	$8 \times 8 \times 12$	70 400	7.7

The LBM simulations of the tumbling particles in Sec. 6 for the domain size of 576^3 lattice sites and 600 000 time steps were performed on LiMa on $8 \times 12 \times 8$ processes and took about 16 h. The runs for the domain size of 768^3 sites with 605 000 time steps were performed on SuperMUC within 48 h. These simulations with periodic boundary conditions are slower than the single particle simulations, due to the

average velocity computation for momentum stabilization that requires global MPI communication.

5. Validation and comparison of the different methods for single particle motion

This section presents a systematic validation of the models, algorithms and the software used. To this end, we describe our findings regarding the motion of a single particle under constant force and torque, respectively, and compare the results obtained from LBM simulations to analytical models for slender bodies in a fluid.

5.1. Analytical formulas

From the analytical formulas for the motion of a slender body in free-space given in Sec. 2.3, theoretical values for the translational and angular velocities of cylinders and ellipsoids are computed. We compare these values to our simulation results for validation of the implementation and used methods.

For a single fiber in a free-space setting the SBF yields explicit formulas for the translational and angular velocity of the fiber. Under a constant force \mathbf{F} or torque \mathbf{M} , Eqns. (23) and (24) simplify to

$$\mathbf{U} = \dot{\mathbf{x}} = \frac{1}{8\pi\mu_f L} [d(\mathbf{I} + \mathbf{t}\mathbf{t}^T) + 2(\mathbf{I} - \mathbf{t}\mathbf{t}^T)]\mathbf{F}, \quad (41)$$

$$\boldsymbol{\omega} = \dot{\mathbf{t}} \times \mathbf{t} = \mathbf{t} \times \frac{3d}{2\pi\mu_f L^3} (\mathbf{M} \times \mathbf{t}), \quad (42)$$

noting that $\mathbf{V}_m = \mathbf{0}$ when there is only one fiber present in the system. These expressions are valid for an ellipsoidal particle of length L and aspect ratio $1/\varepsilon$ represented by the geometry parameter d (see Eqn. (17)) moving in a fluid with dynamic viscosity μ_f . Considering a force either parallel or perpendicular to \mathbf{t} , Eqn. (41) gives

$$\mathbf{U}_{\text{SBF}}^{\parallel} = \frac{2d}{8\pi\mu_f L} \mathbf{F} \quad \text{and} \quad \mathbf{U}_{\text{SBF}}^{\perp} = \frac{d+2}{8\pi\mu_f L} \mathbf{F}. \quad (43)$$

These are the same expressions as derived by Cox for the lengthwise and sidewise motion of a spheroid, see Eqn. (10). For \mathbf{M} perpendicular to \mathbf{t} Eqn. (42) simplifies to

$$\omega_{\text{SBF}} = \frac{3d}{2\pi\mu_f L^3} \mathbf{M}. \quad (44)$$

The friction coefficients for the spherocylinders that we use in the lattice Boltzmann simulation are not known analytically. However, as a first approximation we can compare our data to the analytical results for cylinders and spheroids presented in Sec. 2.3.

The results for the spherocylinders are expected to lie between the results for cylinders of the same radius, but with

²www.rrze.fau.de/dienste/arbeiten-rechnen/hpc/systeme/

³www.lrz.de/services/compute/supermuc/

the length of the spherocylinder without the spherical end-caps L_{nC} ($L_{nC} = L - 2r$, see Fig. 2(a)) and with the full spherocylinder length L .

From the analytical expressions for cylinders derived by Tirado et al., the terminal translational velocity for lengthwise motion can be computed from the friction coefficients in Eqn. (11) with shape-dependent correction factor in Eqn. (13). In case of cylinders of spherocylinder length without the spherical end-caps, it is denoted by $U_{\text{Tir},nC}^{\parallel}$. For cylinders of the full spherocylinder length, the translational velocity is denoted by $U_{\text{Tir},wC}^{\parallel}$.

Analogously, the terminal translational velocity for side-wise motion of cylinders computed from Eqn. (11) with shape-dependent correction factor in Eqn. (14) is denoted by $U_{\text{Tir},nC}^{\perp}$ for the spherocylinder length without end-caps, and $U_{\text{Tir},wC}^{\perp}$ for the full spherocylinder length. The angular velocities computed from Eqn. (7) and Eqn. (12) with the shape-dependent correction factor in Eqn. (15) is denoted by $\omega_{\text{Tir},nC}$ and $\omega_{\text{Tir},wC}$ for the spherocylinder length without end-caps and for the full spherocylinder length, respectively.

5.2. Models and parameters

The parameters used for the validation experiments are chosen based on LBM requirements in terms of spatial and temporal resolution. To sufficiently resolve the particles, the radius of the spherocylinders is kept constant at $r = 4 \text{ dx}$, with spatial discretization $\text{dx} = 10 \cdot 10^{-6} \text{ m}$. The aspect ratios $1/\varepsilon$ are varied from 4 to 14, corresponding to particle lengths L of 16 dx to 56 dx. As a fluid, we choose water at room temperature with kinematic viscosity $\nu_f = 1 \cdot 10^{-6} \text{ m}^2/\text{s}$ and density $\rho_f = 1 \cdot 10^3 \text{ kg/m}^3$, corresponding to the dynamic viscosity $\mu_f = 10^{-3} \text{ kg/(m s)}$. For the LBM $\tau = 6$ is chosen, which results in the time increment $\text{dt} = 183 \cdot 10^{-6} \text{ s}$ by its relation to ν_f and dx given in Eqn. (31).

The spherocylinders are modeled with the density $\rho_p = 1195 \text{ kg/m}^3$. To all these spherocylinders with different aspect ratios the same force $F_z = 5.128 \cdot 10^{-10} \text{ kg m/s}^2$ is applied for the translational velocity validation. This force corresponds to the gravitational force acting on a sphere with $r = 4 \text{ dx}$ for the given density difference between spherocylinders and fluid (see Eqn. (3)). The parameters are chosen such that all simulations are performed with small enough Reynolds number ($\text{Re}_{p,d} \leq 0.040$) so that we are in the Stokes regime. The obtained particle Reynolds numbers defined in Eqn. (4) for the terminal sedimentation velocity of the spherocylinders are in the range of $\text{Re}_{p,d} = 0.016 \dots 0.040$ (see Tab. A.7, Appendix A). Higher aspect ratios than $1/\varepsilon = 14$ are difficult to simulate with the LBM at very low Reynolds numbers, due to large domain sizes required to reduce wall effects (see Sec. 5.4) and decreasing dt required with increasing particle lengths (see Eqns. (4), (31) and (29)).

For the rotational motion validation the torques in Tab. 2 acting in x-direction are applied, leading to a rotation of the spherocylinder axis in the x-z plane. These torques are chosen such that the theoretical tip velocity $u_{\text{tip}} = 1 \cdot 10^{-8} \text{ m/s}$ is the same for all aspect ratios. This velocity is computed as $u_{\text{tip}} = \omega_{\text{Tir},wC} L/2$, i.e. from the angular velocity according to Eqn. (12) for a cylinder with the spherocylinder length including the end-caps. The corresponding theoretical particle Reynolds number is $\text{Re}_{p,d} = 0.009$. The Reynolds numbers obtained in the simulations in this case are $\text{Re}_{p,d} = 0.013 \dots 0.010$ for $1/\varepsilon = 4 \dots 14$ (see Tab. A.7).

Table 2. Torques M_x in $10^{-15} [\text{kgm}^2/\text{s}^2]$ applied to spherocylinders of different aspect ratios $1/\varepsilon$ for rotational velocity validation.

$1/\varepsilon$	4	6	8	10	12	14
M_x	12.26	17.86	24.62	32.38	41.09	50.68

For the LBM simulations, the particles are placed in large domains to minimize the wall influence and to make the results comparable to free space. The translational velocity validation with the LBM is performed in a cuboid domain with free-slip boundary conditions applied at the walls. The size of the domain in the direction of motion is elongated and denoted by L_z . In the other dimensions it has the same size, i.e., $L_x = L_y$. Initially, the spherocylinder is placed at the center w.r.t. the x - and y -dimension, and at a distance of $z = 100 r$ from the top boundary of the domain located at $z = 0$. Here, the coordinate system depicted in Fig. 2(a) is used, and a slice through the simulation domain center along the x-z plane is shown in Fig. 8. Under the influence of F_z , the spherocylinder is then moving downwards along the domain centerline in positive z -direction.

For validation of the rotational velocity, the spherocylinder is placed at the center of a cubic domain, and the torques M_x from Tab. 2 are applied constantly. Since these torques act in tangential direction to the domain boundaries, no-slip boundary conditions are applied at the walls to prevent the fluid from accelerating infinitely. The same setups are used for studying the influence of the wall on the terminal motion and for the flowfield visualization.

5.3. Single particle motion results

We validate the LBM by comparing the spherocylinder velocities to analytical solutions according to the theories of Cox and Tirado et al. for cylinders, as well as the SBF for ellipsoids. Moreover, the influence of the particle shape, fluid inertia, and wall effects on the particle velocities is investigated for the different methods and theories.

For the translational velocity validations, the simulations are performed for the domain size $[2560 \text{ dx}]^2 \times 2688 \text{ dx}$ for 37 000 to 64 400 time steps for the lengthwise moving particles, and for 56 200 to 88 800 time steps for the sidewise

motion. A high number of time steps is required until the particles reach steady-state—the longer the particles are, the more time steps are needed. For the validation of the angular velocity, the LBM simulations are performed for the domain size $[816 \text{ dx}]^3$ and 40 000 to 140 000 time steps.

The sedimentation velocities for lengthwise and sidewise motion are shown in Fig. 3 and Fig. 4, respectively, for spherocylinders, cylinders, and ellipsoids with different aspect ratios. The angular velocities are presented in Fig. 6. For the considered aspect ratios, the analytical expressions by Tirado et al. are the most accurate, whereas the asymptotic expressions by Cox and the SBF are valid for very high aspect ratios (see Sec. 2.3). Thus, the obtained velocities are normalized by the solutions $U_{\text{Tir,wC}}$ and $\omega_{\text{Tir,wC}}$ of Tirado et al. for cylinders of the full particle length, in order to highlight the differences in the velocities.

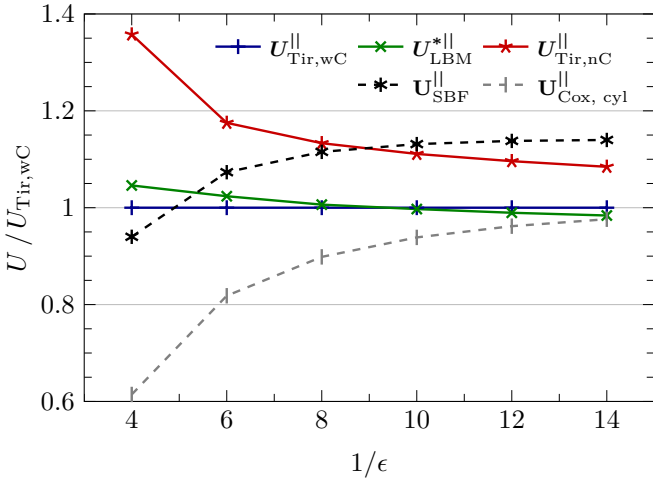


Figure 3. Normalized sedimentation velocities $U/U_{\text{Tir,wC}}$ for lengthwise orientation w.r.t. direction of force $F_z = 5.128 \cdot 10^{-10} \text{ kg m/s}^2$ for aspect ratios $1/\epsilon$ and radius $r = 4 \text{ dx}$. Comparison of LBM velocities (U_{LBM}^*) in $[2560 \text{ dx}]^2 \times 2688 \text{ dx}$ sized domain with free-slip boundaries, to free-space solutions by Tirado for cylinders of lengths including ($U_{\text{Tir,wC}}^||$) and excluding ($U_{\text{Tir,nC}}^||$) spherocylinder end-caps, and to Cox ($U_{\text{Cox,cyl}}^||$) and SBF ($U_{\text{SBF}}^||$) for cylinders and ellipsoids of full spherocylinder lengths, respectively.

In the figures, terminal sedimentation velocities from the previously described LBM simulations for lengthwise ($U_{\text{LBM}}^*||$), sidewise ($U_{\text{LBM}}^*\perp$), and rotational (ω_{LBM}^*) motion are plotted, normalized by the corresponding Tirado velocities. For comparison, the normalized velocities according to Tirado et al. for cylinders of the same total length (denoted by subscript ‘Tir,wC’), and for the spherocylinder length without the spherical end-caps are shown (‘Tir,nC’), together with the Cox results (‘Cox, cyl’) for cylinders and the SBF results (‘SBF’).

The LBM results in Fig. 3 to Fig. 6 are mean values of particle velocities after a sufficient number of time steps so that steady state is reached with sufficient accuracy. Due to obstacle mapping effects, the particle velocities fluctu-

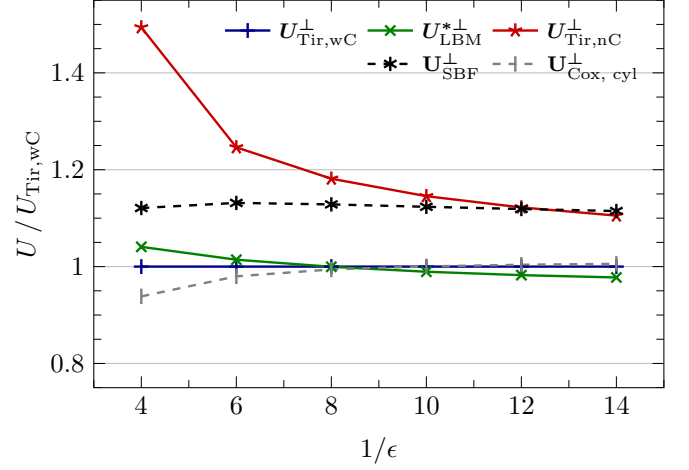


Figure 4. Normalized sedimentation velocities $U/U_{\text{Tir,wC}}$ for orientation perpendicular to F_z , $r = 4 \text{ dx}$, and aspect ratios $1/\epsilon$. Comparison of LBM velocities ($U_{\text{LBM}}^*\perp$) in $[2560 \text{ dx}]^2 \times 2688 \text{ dx}$ domain with free-slip boundaries, to free-space solutions by Tirado ($U_{\text{Tir,wC}}^perp$, $U_{\text{Tir,nC}}^perp$), Cox ($U_{\text{Cox,cyl}}^perp$), and SBF (U_{SBF}^perp).

ate as the effective particle volume varies with the number of overlapped particle cells (see Sec. 4.2). The mean values U_{LBM}^* and ω_{LBM}^* are computed from the velocities sampled every 200 time steps. For the validation of translational velocity, the last 15% of these velocity values are considered and the last 50% for the validation of the angular velocity that converges to steady state more quickly.

The fluctuations are computed from the minimum and maximum values of the considered velocities as $\delta_U = (U_{\text{max}}^* - U_{\text{min}}^*)/U_{\text{LBM}}^*$ and δ_ω , analogously. The fluctuations for the translational motion are lower than for the rotational motion. For sidewise moving spherocylinders, fluctuations of $\delta_U = 0.8\%$ occur for all aspect ratios. For the lengthwise moving spherocylinders, the fluctuations correspond to a value of $\delta_U = 0.8\%$ for $1/\epsilon = 4$ and decrease with increasing particle length. For the rotational motion, fluctuations of $\delta_\omega = 8\%$ arise for $1/\epsilon = 4$ and decrease to $\delta_\omega = 2.8\%$ for the longest examined particle. Exact figures of the fluctuations are given in Tab. A.7 (Appendix A), together with figures of the LBM results and associated Reynolds numbers, of the analytical solutions according to Tirado et al. and of the relative deviations $\Delta_r U = (U_{\text{LBM}}^* - U_{\text{Tir}})/U_{\text{Tir}}$ and $\Delta_r \omega$ (defined analogously) of the LBM results from the Tirado velocities.

The terminal velocities for translational motion of spherocylinders in Fig. 3 and Fig. 4 are close to the cylinder velocities according to Tirado for full spherocylinder lengths. For small aspect ratios $1/\epsilon \leq 8$ the spherocylinder velocities are slightly higher than $U_{\text{Tir,wC}}$ and are thus closer to those of cylinders with the length of the spherocylinder without the end-caps. The LBM velocity for $1/\epsilon = 4$ is by $\Delta_r U = 4.6\%$ higher than $U_{\text{Tir,wC}}$ for lengthwise motion and by 4.1% for sidewise motion (see Tab. A.7). For large aspect ratios, the LBM sedimentation velocities

are slightly lower than the analytical solutions $U_{\text{Tir,wC}}$ for cylinders. The LBM velocity for the highest aspect ratio is by $\Delta_r U = 1.6\%$ lower than $U_{\text{Tir,wC}}$ for lengthwise motion and by 2.3% for sidewise motion.

The lower spherocylinder velocities for $1/\varepsilon \geq 10$ result from wall effects that slow down the particles compared to a free-space setting. These effects are examined more closely in Sec. 5.4. The wall influence is higher for sidewise orientation, resulting in LBM results and the Tirado results $U_{\text{Tir,wC}}$ to coincide for the lower aspect ratio of $1/\varepsilon = 8$, compared to $1/\varepsilon = 10$ for lengthwise orientation.

Inertial effects are included in the LBM simulations and result in lower sedimentation velocities compared to Stokes flow since the fluid resistance increases with Reynolds number. For both, lengthwise and sidewise motion, the LBM velocities U_{LBM}^* are higher than $U_{\text{Tir,wC}}$ only for low aspect ratios, i.e., for minimal Reynolds numbers based on the particle length. For long particles U_{LBM}^* is lower than $U_{\text{Tir,wC}}$, and thus inertia might play an additional role in the translational motion simulations.

For both orientations, the velocities according to Cox and the SBF exhibit a similar behavior for small aspect ratios. Both velocities increase at the same rate with increasing particle lengths for low aspect ratios and slowly decrease for higher aspect ratios. However, while Cox' results quickly converge to values close to the Tirado velocities, the SBF velocities of ellipsoids stay higher. For $8 \leq 1/\varepsilon \leq 14$, the SBF velocities are by 10 – 15% higher than the results by Tirado. This effect can be attributed to

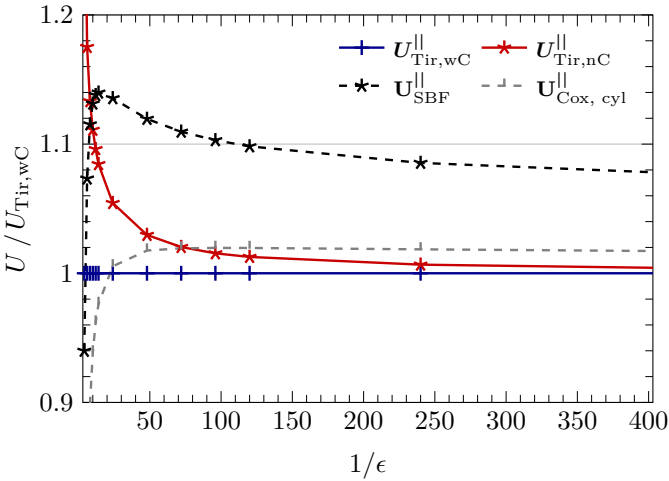


Figure 5. Normalized sedimentation velocities $U/U_{\text{Tir,wC}}$ for lengthwise orientation w.r.t. F_z for $r = 4dx$ and high aspect ratios $1/\varepsilon$. Comparison of theories for cylinders by Tirado ($U_{\text{Tir,wC}}^{\parallel}$, $U_{\text{Tir,nC}}^{\parallel}$) and Cox ($U_{\text{Cox,cyl}}^{\parallel}$) and for ellipsoids by the SBF ($U_{\text{SBF}}^{\parallel}$).

the different particle shapes, which becomes clear in Fig. 5 that shows the velocities according to the different theories for lengthwise motion at higher aspect ratios than simu-

lated with the LBM. Here, the SBF velocities of ellipsoids are first higher than the velocities according to Tirado for $1/\varepsilon \geq 8$ and converge only very slowly towards the results for cylinders. For sidewise motion the differences between the theories are smaller, and the associated velocities converge faster than for the lengthwise motion, due to a lower dependence on the particle shape.

For the rotational motion of elongated particles shown in Fig. 6 the differences between the theories and methods are larger than for translational motion. Also the Tirado re-

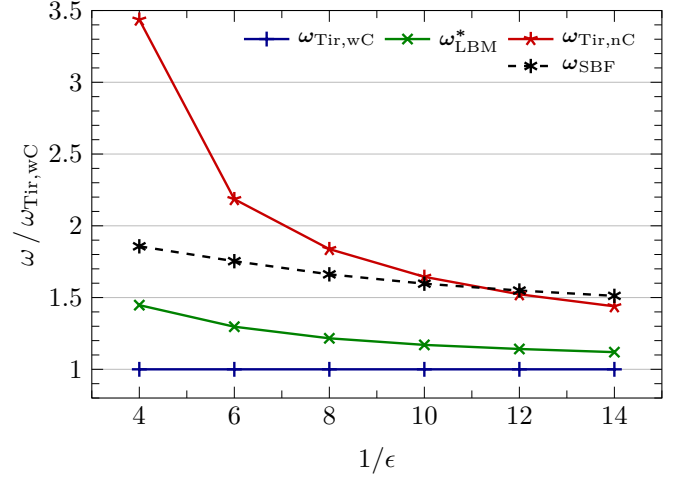


Figure 6. Normalized angular velocities $\omega/\omega_{\text{Tir,wC}}$ of particles with $r = 4dx$ and aspect ratios $1/\varepsilon$, resulting from torques M_x in Tab. 2. Comparison of LBM velocities (ω_{LBM}^*) in $[816dx]^3$ domain with no-slip boundaries, to free-space solutions by Tirado ($\omega_{\text{Tir,wC}}$, $\omega_{\text{Tir,nC}}$) and the SBF (ω_{SBF}).

sults depend more strongly on the particle length. As for translational motion, the velocity according to the SBF is higher than the Tirado solution for cylinders with full spherocylinder length. The angular velocities of the spherocylinders from the LBM simulations lie between the solutions for cylinders of a length with and without the end-caps for all aspect ratios. Again, the LBM velocities are closer to the values of a cylinder of the full spherocylinder length. However, the relative deviation from $\omega_{\text{Tir,wC}}$ is significantly higher than for the translational motion. For $1/\varepsilon = 4$, $\Delta_r \omega = 45\%$ and for $1/\varepsilon = 14$ still $\Delta_r \omega = 12\%$. With increasing aspect ratio, the LBM velocities more closely approach the Tirado velocities with the full spherocylinder length than the SBF results do. The angular velocities by the SBF exceed the Tirado results by almost 90% for $1/\varepsilon = 4$ and still by more than 50% for $1/\varepsilon = 14$. The wall influence is negligible for rotational motion, as shown in Sec. 5.4. With increasing particle length, the angular LBM velocities ω_{LBM}^* decrease towards $\omega_{\text{Tir,wC}}$. Thus, also for rotational motion the LBM results might be influenced by inertial effects that lead to lower velocities, in addition to the higher hydrodynamic similarity of longer spherocylinders and cylinders of same length.

5.4. Wall influence in LBM simulations

The influence of the wall effect in the LBM simulations on the settling velocity of spherocylinders is examined for domains with quadratic cross-section of $L_x = L_y := (160, 320, 480, 640, 832)$ dx and constant length $L_z = 1200$ dx, and with sizes $[1280 \text{ dx}]^2 \times 1600 \text{ dx}$, $[1920 \text{ dx}]^2 \times 2240 \text{ dx}$, and $[2560 \text{ dx}]^2 \times 2688 \text{ dx}$. The simulations investigating the wall influence on rotational motion are performed for cubic domains with edge lengths of $(168, 324, 480, 648, 816, 1296)$ dx. For the aspect ratios $1/\varepsilon = 8$ and $1/\varepsilon = 12$, 80 000 and 84 000 time steps are performed, respectively.

The terminal translational and rotational velocities are presented in Fig. 7 on the left and right ordinate, respectively, dependent on $L_x = L_y$ plotted as ' $L_{x,y}$ ' on the abscissa. The displayed velocities are again the mean values of the particle velocities evaluated every 200 time steps. For the translational motion, the last 34% of these velocities are considered, and the last 15% for the largest domain only. For the rotational motion, the last 50% are considered.

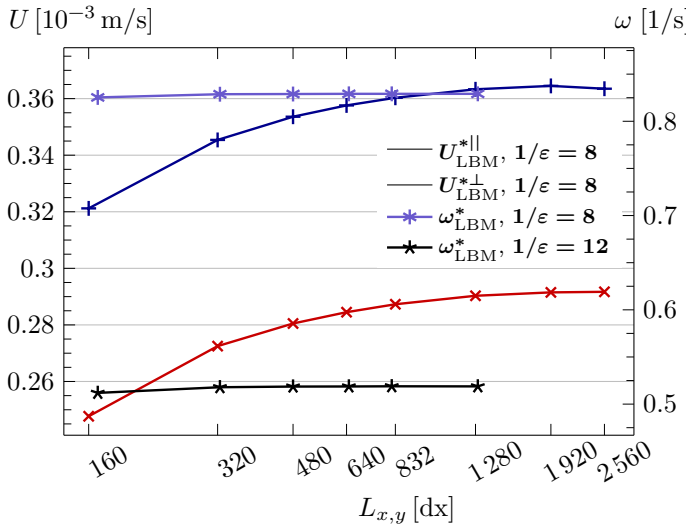


Figure 7. Sedimentation and rotation velocities of spherocylinders with radius $r = 4$ dx and aspect ratio $1/\varepsilon = 8$ —and $1/\varepsilon = 12$ for rotation—from LBM simulations in water-filled domains of different sizes ($L_{x,y}$). Domains for the sedimentation velocities of lengthwise ($U_{LBM}^{*||}$) and perpendicular ($U_{LBM}^{*\perp}$) oriented spherocylinders (w.r.t. force F_z) are cuboids with free-slip boundaries, and cubes with no-slip boundaries for the angular velocities (ω_{LBM}^{*}) resulting from torques M_x in Tab. 2.

The terminal translational velocities of the spherocylinders with $1/\varepsilon = 8$ in Fig. 7 increase significantly with domain size. For the translational motion of lengthwise oriented spherocylinders, the retarding effect of the confined domain on the sedimentation velocity is negligible for domain sizes of $[1280 \text{ dx}]^2 \times 1600 \text{ dx}$ and above. For sidewise oriented particles, only the $[2560 \text{ dx}]^2 \times 2688 \text{ dx}$ domain is sufficiently large to assume negligible wall effects. These

findings confirm the statement in Sec. 5.3 that the wall effect is measurable for $1/\varepsilon \geq 10$ in the $[2560 \text{ dx}]^2 \times 2688 \text{ dx}$ domain, and that the corresponding velocities are underestimated.

For the rotational motion, there is hardly any impact of the confined domains on the angular velocities for both aspect ratios $1/\varepsilon = 8$ and $1/\varepsilon = 12$. Thus, the wall effect for the $[816 \text{ dx}]^3$ domain in Sec. 5.3 is negligible for all considered aspect ratios. According to the angular velocities shown in Fig. 7, domains with edge length 480 dx and 648 dx are sufficient for $1/\varepsilon = 8$ and $1/\varepsilon = 12$, respectively.

5.5. Flow field around sedimenting particles

We present the flow field around a single sedimenting spherocylinder in a closed domain with free-slip boundary conditions simulated with the LBM. The simulations are performed for spherocylinders of aspect ratio $1/\varepsilon = 12$ in a domain of size $[832 \text{ dx}]^2 \times 1200 \text{ dx}$ for 74 800 time steps. The fluid velocity around the sedimenting spherocylinder and the staircase-approximated spherocylinder itself depicted in Fig. 8 are visualized with ParaView. The flow field around the spherocylinder is shown along the x-z plane through the domain center for a particle oriented lengthwise and sidewise along the direction of the applied force F_z in Fig. 8(a) and Fig. 8(b), respectively. Since the velocity magnitude decays quickly with increasing distance from the spherocylinders, white isosurface contour lines indicate the velocity magnitude with logarithmic contour intervals. The flow direction is depicted by small streaks of uniform length. The sixteen contour lines are plotted for both orientations at velocity magnitudes in the range of $304 \cdot 10^{-6} \text{ m/s}$ to $304 \cdot 10^{-12} \text{ m/s}$.

The initially quiescent fluid is dragged along by the spherocylinder and starts moving adjacent to the particle. Along the channel centerline a fluid flow develops in the direction of spherocylinder motion. The walls in z-direction cause a counterflux and thus a vortex. Initially the vortex is located next to the particle and then moves to a position half-way between particle surface and confining walls. For the lengthwise oriented spherocylinder in Fig. 8(a), the contour lines have a similar shape as the particle. For the sidewise oriented spherocylinder in Fig. 8(b), the contour lines next to the particle are circular, and they have similar shape as for the lengthwise oriented spherocylinder in some distance. However, the shape is more circular, i. e., the flow is influenced to a higher degree also orthogonal to the movement direction. Moreover, the sidewise moving spherocylinder influences the fluid at larger distances than the lengthwise oriented spherocylinder, as can be seen from the distance of equivalent contour lines to the particles.

In accordance with the results in Sec. 5.3, the particle with sidewise orientation moves slower than for lengthwise orientation. The same position in movement direction is

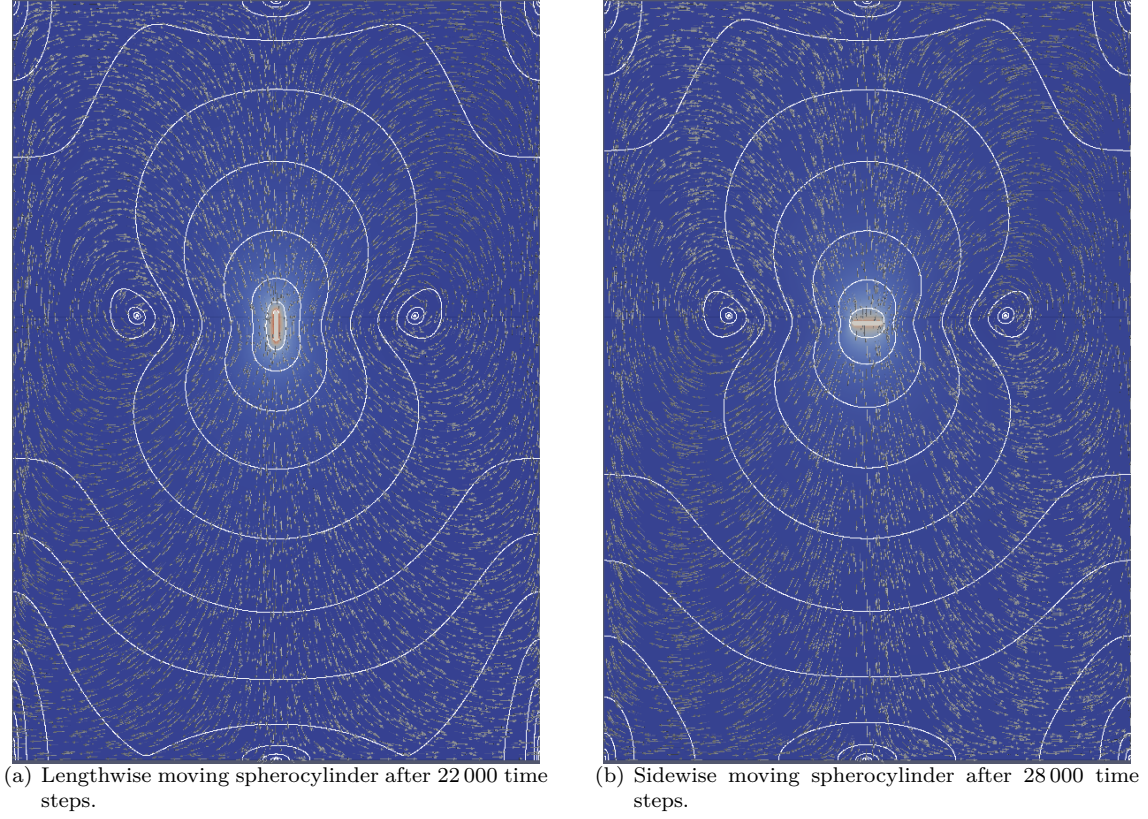


Figure 8. Flow around sedimenting spherocylinders along x-z plane through domain center. Flow direction is indicated by small streaks, and velocity magnitude by color in range of $360 \cdot 10^{-6}$ m/s (red) to 0 m/s (blue) and logarithmic contour lines.

reached after 22 000 time steps for lengthwise orientation, and after 28 000 time steps for sidewise motion.

The flow field caused by the sidewise moving spherocylinder is nearly equal in both directions orthogonal to the movement direction. Only very close to the spherocylinder, the fluid velocity in x-z plane shown in Fig. 8(b) is found to be slightly higher than in the orthogonal y-z plane.

6. Tumbling particles

In this section we study the tumbling motion of two elongated particles in a periodic domain. We present simulation results for spherocylinders with the LBM, as well as SBF results for ellipsoidal fibers. A comparison of the results from the two methods is presented for different domain sizes and aspect ratios. For the LBM, the influence of the initial particle distance on the tumbling behavior is examined.

6.1. Setup and parameters

The LBM simulations are performed with two spherocylinders of radius $r = 4$ dx, with $dx = 4.98 \cdot 10^{-6}$ m. The particle length, L , is varied between 40 dx and 56 dx, cor-

responding to the aspect ratios $1/\varepsilon = 10$ to $1/\varepsilon = 14$. Initially the particles are placed, aligned with the direction of gravity, in a periodic box at the center w.r.t. y-direction and centered around the middle of the domain in x-direction with a given center-to-center distance *dist* w.r.t. the coordinate system depicted in Fig. 2(a). The dimensions of the box are 576 dx or 768 dx in all three directions, i.e. $L_x = L_y = L_z$. For the smaller domain, 600 000 time steps are performed and for the larger domain 605 000 time steps. To keep the system from accelerating infinitely due to the constantly applied force, the momentum stabilization technique described in Sec. 4.1 is applied.

As fluid, we model water at room temperature, with the kinematic viscosity ν_{f,H_2O} and the density ρ_{f,H_2O} from Sec. 5.2. The density of the particles is set to $\rho_p = 1492$ kg/m³. The force acting on the particles in z-direction caused by gravity results in the values presented in Tab. 3.

Table 3. Gravitational forces applied to the particles of different aspect ratios $1/\varepsilon$ in z-direction for the tumbling simulations.

$1/\varepsilon$	10	12	14
F_z [10^{-9} kg m/s ²]	1.119	1.358	1.598

The resulting particle Reynolds number $Re_{p,d}$ for the par-

ticles based on the mean sedimentation velocity U^* for the LBM lies in the range 0.052 to 0.063 for $1/\varepsilon = 10$ and $1/\varepsilon = 14$, respectively (see Tab. 5), so that we are essentially in the Stokes regime. For the LBM simulations, we apply the relaxation time $\tau = 6$ that results in the time increment $dt = 4.55 \cdot 10^{-5}$ s (see Eqn. (31)).

In the SBF we use the following parameters $N = 5$, 48 quadrature points along the fiber (see Eqn. (22)), and $dt \approx 0.003$ s.

An SBF simulation with 8300 time steps (TS) was performed within 66.40 s on a single core of an Intel Core i7 4770 processor running at 3.4 GHz, i.e., with 125 TS/s. The parallel runtimes for the LBM on 768 cores given in Sec. 4.4 correspond to 10.4 TS/s on LiMa and 3.5 TS/s on SuperMUC.

6.2. Flow field around tumbling spherocylinders

We present the flow field around two tumbling spherocylinders simulated with the LBM in a periodic domain of size $[576 dx]^3$, filled with water. The setup and parameters described in Sec. 6.1 are used for spherocylinders of aspect ratio $1/\varepsilon = 12$ and an initial center-to-center distance of 16 dx, with $dx = 4.98 \cdot 10^{-6}$ m.

In Fig. 9 the flow field is visualized along a slice in the x-z plane through the domain center. The velocity magnitude is represented by a color range from red to blue and by (sixteen) white isosurface contour lines of logarithmic intervals in the range of $2.60 \cdot 10^{-3}$ m/s to $96.1 \cdot 10^{-9}$ m/s. The flow direction is represented by streaks of uniform length. In addition to the image sequence in Fig. 9, an animation is available via a permalink⁴.

At the beginning of the tumbling period, both particles are aligned with the external force direction (see Fig. 9(a)), and then start rotating (see Fig. 9(b)). As the particles rotate, they move apart in x-direction until they are oriented perpendicular to the force (see Fig. 9(c)) and reach the maximum distance. The rotation continues, and the particles move further along the force direction (see Fig. 9(d)) until the next period begins. A more detailed description of the particle positions and velocities is given in Sec. 6.3. The fluid is dragged along with the spherocylinders, while the flow velocity quickly decreases with increasing distance from the particles. As expected, the flow field is at all times symmetric w.r.t. the domain center in x- and y-direction and changes in z-direction. During the tumbling motion, two vortices are forming at the same height (i.e., z-coordinate) as the particle center. Half-way between periodically following particles in z-direction, a region of zero flow velocity appears at the interface of two vortices associated with these periodically neighboring particles. As the particles change their mutual distance, the vortices and the zero flow velocity regions only slightly change their positions in x-direction.

6.3. Tumbling results for spherocylinders using LBM

We examine the dependence of the tumbling motion on the spherocylinder aspect ratio, the domain size, and the initial distance between the particles. The influence of the aspect ratio on the tumbling behavior is analyzed for spherocylinders with $1/\varepsilon = 10$, $1/\varepsilon = 12$, and $1/\varepsilon = 14$. For one particle, the position in x-direction and its velocity in x- and z-direction are presented in Fig. 10 over time. The simulations are performed for the domain size $[576 dx]^3$ and the initial center-to-center particle distance of 16 dx in x-direction.

Initially, the particles move away from the domain center and from each other in x-direction. Once the maximal distance is reached, the particles move back towards each other. This motion is repeated periodically. While the particles aligned with the direction of gravity move apart, the velocity in x-direction increases, and the particles start rotating. Before the particles are oriented perpendicular to the gravitational direction, the maximal velocity in x-direction is reached, and the particle velocity in x-direction decreases again. The velocity in x-direction becomes zero once the particles are oriented perpendicular to gravity. While the particles continue rotating, the velocity in x-direction becomes negative, i.e., the particles approach each other. The velocity in negative x-direction increases at first and then decreases again as the particles rotate further. Once the particles are aligned with the direction of gravity, the velocity in x-direction is zero again, and the minimal separation is reached. In z-direction, the maximal velocity occurs when the particles are oriented with the direction of gravity and the particle distance is minimal. The minimal velocity in z-direction is reached when the particles are oriented perpendicular to the direction of gravity and the particle distance is maximal. In both cases, the velocity in x-direction is zero. The values for the y-direction are not shown since the particles move in the x-z plane, keeping their y-coordinate.

The maximal separation in x-direction, the maximal velocity magnitude in this direction, and the sedimentation velocity in z-direction all depend on the particle length. With increasing particle length, the terminal maximal separation distance, the maximal velocity magnitude in x-direction, and the sedimentation velocity u_z increase. The minimal separation is nearly equal for all particle lengths. For $1/\varepsilon = 10$, the maximal separation distance per period is small at first and then increases over many periods, while for $1/\varepsilon = 12$ this distance increases only slightly, and the terminal separation distance is reached after five revolutions. For $1/\varepsilon = 14$, the separation distance is relatively high in the first period and then decreases until the terminal distance is reached after approximately three revolutions. Before examining these dependencies further, we analyze how the parameters depend on the initial separation distance between the particles and on the domain size.

⁴<https://www10.cs.fau.de/permalink/eethegh4sh>

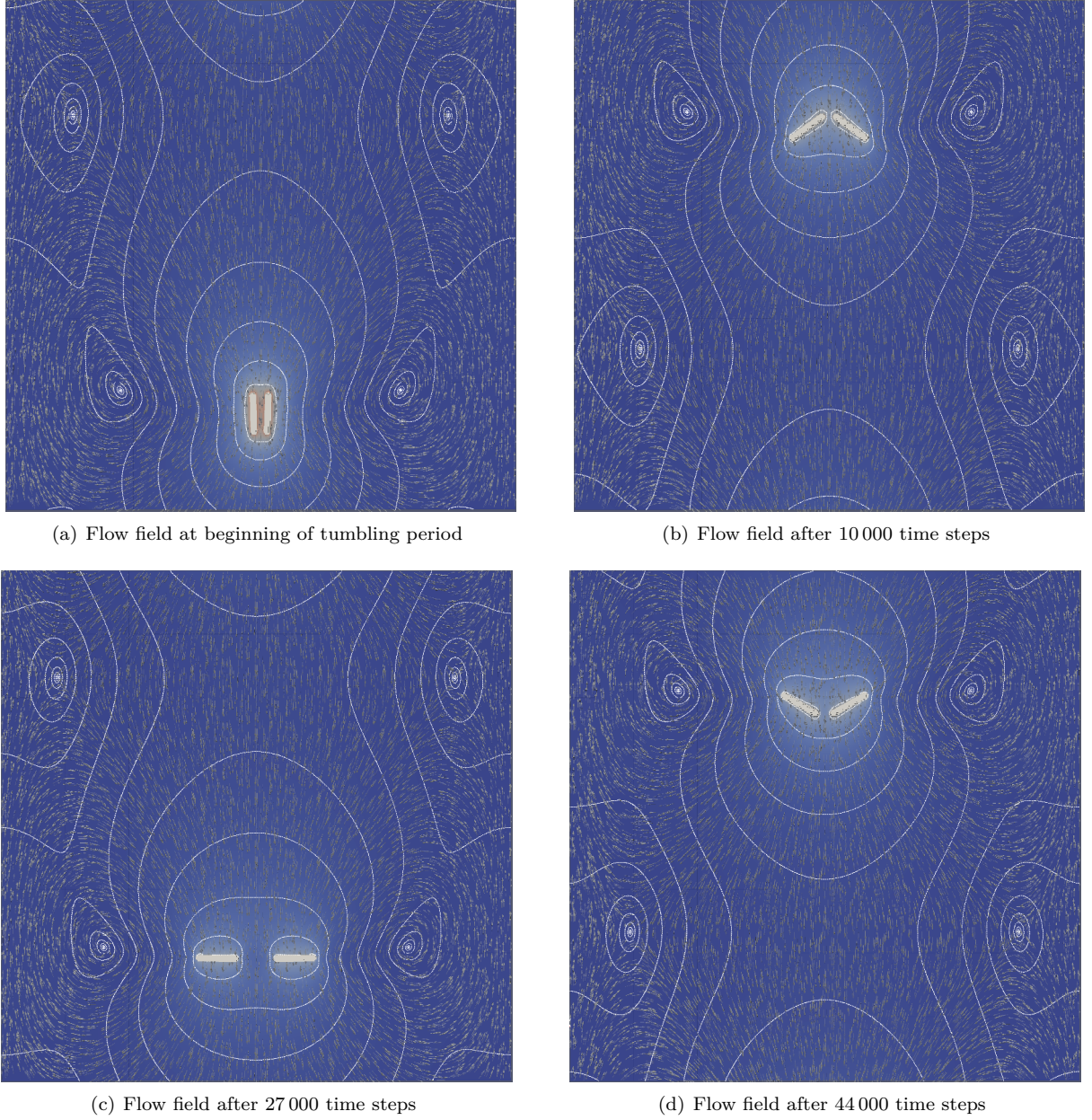


Figure 9. Flow field around two tumbling spherocylinders with radius $r = 4dx$ ($dx = 4.98 \cdot 10^{-6}$ m) and initial distance $16dx$ in periodic domain of size $[576dx]^3$. Flow direction is indicated by streaks, and velocity magnitude logarithmic contour lines and color in range of $3.16 \cdot 10^{-3}$ m/s (red) to $20 \cdot 10^{-9}$ m/s (blue).

In Fig. 11 we present LBM results for the tumbling motion of particles with aspect ratio $1/\varepsilon = 12$ for a smaller initial center-to-center distance of $14.8dx$. Moreover, we compare the particle motion for the previous domain size $[576dx]^3$ and a larger domain of size $[768dx]^3$. All the other parameters are kept the same as for the previous simulations. The particle motion conforms to the previously described behavior for the different aspect ratios. The smaller initial distance of the particles leads to a smaller maximal separation at the beginning of the simulation. Also the tumbling period time is at first smaller than for the higher initial distance. The velocity in x-direction

does not depend on the initial distance, only the sedimentation velocity is a bit higher at first. After a few periods, however, the tumbling motion for the different initial separations no longer differs.

When the domain size is increased from $576dx$ to $768dx$, the particle motion in x-direction is not affected. I.e., the size $576dx$ suffices for negligible mutual influence of the periodically neighboring particles in x-direction. Only in z-direction the velocity is smaller for the larger domain, due to the periodic boundaries.

Among the LBM tumbling simulations presented in this

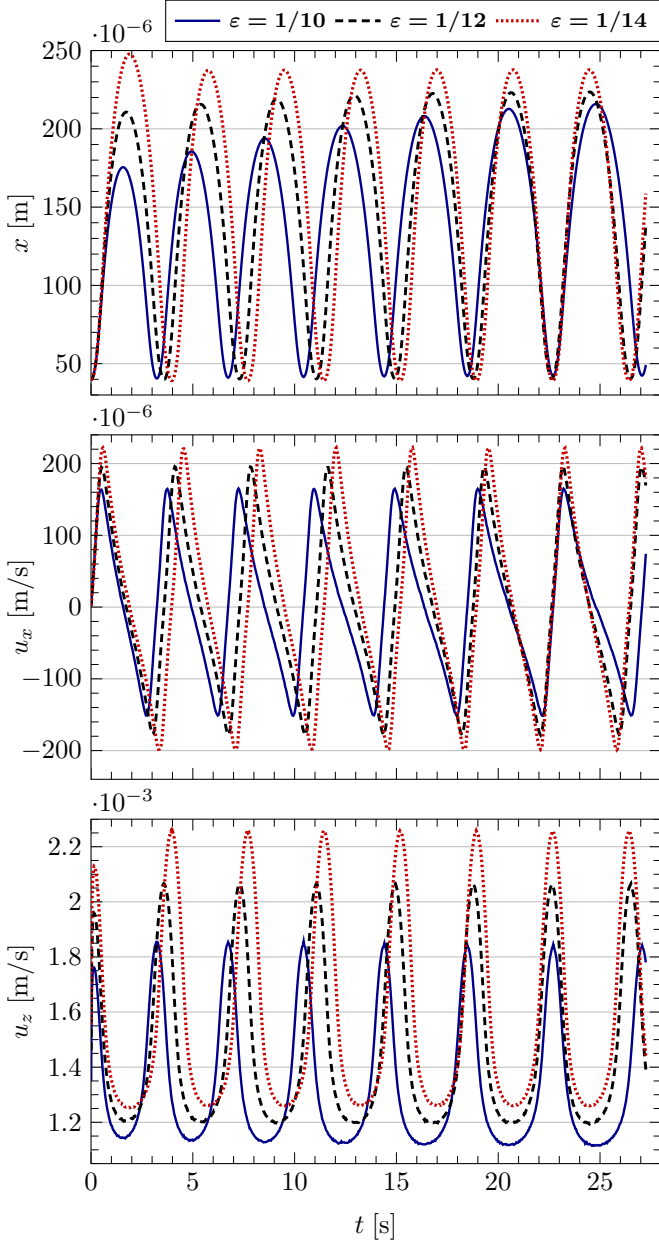


Figure 10. LBM results for tumbling motion of two spherocylinders with radius $r = 4 \text{ dx}$ ($\text{dx} = 4.98 \cdot 10^{-6} \text{ m}$) and aspect ratios $1/\varepsilon = 10$, $1/\varepsilon = 12$, and $1/\varepsilon = 14$ in periodic domain of size $[576 \text{ dx}]^3$ filled with water. Shown are the position of one particle in x-direction and the particle velocities in x- and z-direction over time. The spatial discretization is $\text{dx} = 4.98 \cdot 10^{-6} \text{ m}$, and the initial particle distance is 16 dx .

section, the change in separation distance is the highest for $1/\varepsilon = 10$, and for $1/\varepsilon = 12$ with initial distance 14.8 dx . For these simulations, the measured tumbling period time T^* and period distance D^* in z-direction, and the resulting mean sedimentation velocity U^* are shown in Tab. 4. For both aspect ratios, the tumbling period distance increases as the particles move apart in x-direction. The tumbling period time increases at almost the same rate, leading to

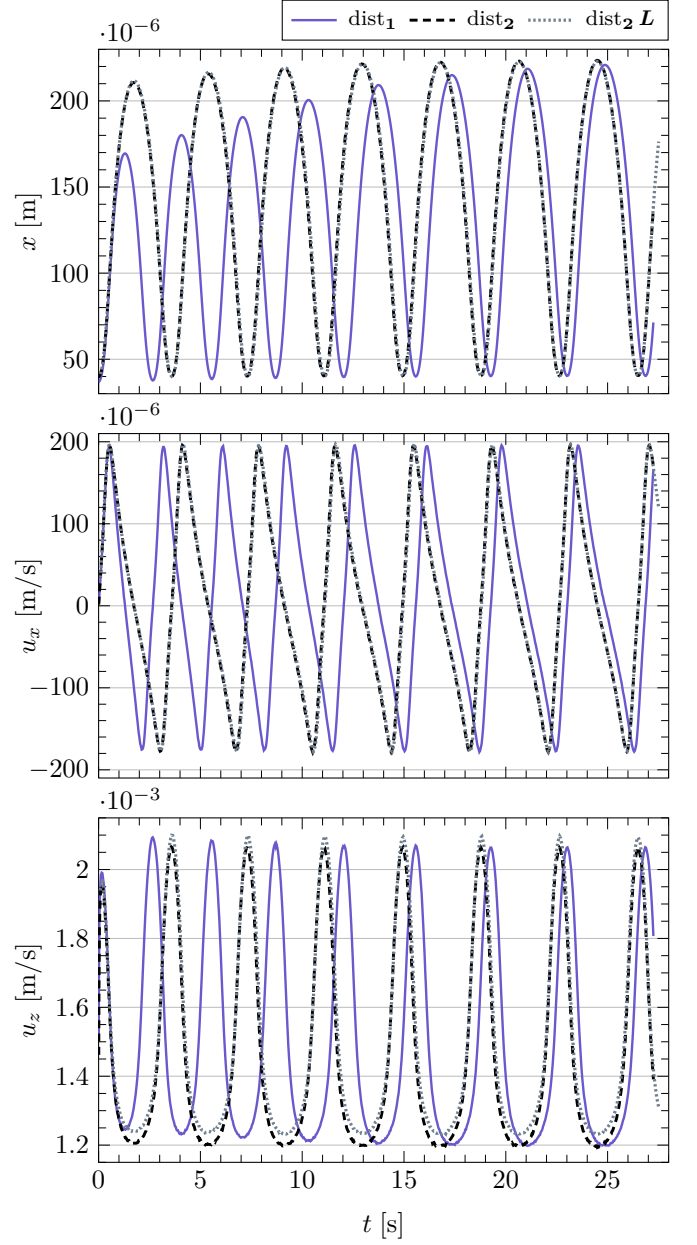


Figure 11. LBM results for tumbling motion of two spherocylinders with radius $r = 4 \text{ dx}$ and aspect ratio $1/\varepsilon = 12$, for initial particle distances $\text{dist}_1 = 14.8 \text{ dx}$ and $\text{dist}_2 = 16 \text{ dx}$ in water-filled periodic domains of size $[576 \text{ dx}]^3$ and $[768 \text{ dx}]^3$. The larger domain is indicated by ‘L’.

an only slightly decreasing mean sedimentation velocity in both cases. The terminal sedimentation velocity for $1/\varepsilon = 12$ is higher than for $1/\varepsilon = 10$.

The main characteristic parameters for the tumbling motion of two spherocylinders obtained from the LBM simulations are summarized in Tab. 5. The terminal mean sedimentation velocity U^* per period rises with increasing aspect ratio or particle length, which agrees with the experimental results in [5]. This behavior is contrary to

Table 4. Changes in sedimentation distance (D^*) per period, period time (T^*), and mean sedimentation velocity (U^*) for different periods of two tumbling particles with radius $r = 4 \text{ dx}$ ($\text{dx} = 4.98 \cdot 10^{-6} \text{ m}$). LBM results for particles with $1/\varepsilon = 10$ and initial distance 16 dx, and for $1/\varepsilon = 12$ with initial distance 14.8 dx in periodic domain of size $[576 \text{ dx}]^3$.

$1/\varepsilon$ period #	1	2	3	4	5	6	7
10 $D^* [10^{-3} \text{ m}]$	4.38	4.78	4.97	5.25	5.41	5.54	5.72
$T^* [\text{s}]$	2.71	3.52	3.69	3.94	4.09	4.23	4.35
$U^* [10^{-3} \text{ m/s}]$	1.61	1.36	1.35	1.33	1.32	1.31	1.31
12 $D^* [10^{-3} \text{ m}]$	4.18	4.50	4.75	5.02	5.24	5.42	5.51
$T^* [\text{s}]$	2.13	2.92	3.08	3.34	3.53	3.70	3.76
$U^* [10^{-3} \text{ m/s}]$	1.96	1.54	1.54	1.50	1.49	1.47	1.47

the sedimentation results in Sec. 5, where the same force is applied to all particles and can thus be attributed to the increasing gravitational force acting on the particles. For the larger domain, U^* increases slightly, as observed previously for u_z . While the terminal mean sedimentation velocity is reached for all simulations, the tumbling period distance D^* and time T^* still change for $1/\varepsilon = 10$ and for $1/\varepsilon = 12$ with $\text{dist} = 14.8 \text{ dx}$ (see also Tab. 4). For the latter, the values converge towards the results for $\text{dist} = 16 \text{ dx}$. The period time decreases with increasing aspect ratio, whereas no clear trend is recognizable for D^* . For the larger domain and $1/\varepsilon = 12$, the smaller sedimentation velocity results mainly from an increased distance D^* .

The velocities in x-direction are significantly smaller than the sedimentation velocities. As reported above, the maximal velocity magnitudes in x-direction increase with particle length. However, these velocities do not depend on the domain size and the initial separation distance. The maximal magnitude $u_{x, \max}$ when the particles separate is higher than the magnitude $u_{x, \min}$ for the approaching

Table 5. Parameters obtained from LBM simulations of two tumbling particles with radius $r = 4 \text{ dx}$ ($\text{dx} = 4.98 \cdot 10^{-6} \text{ m}$) in periodic cubic domain filled with water. Sedimentation distance (D^*), period time (T^*), and mean velocity (U^*) in z-direction, minimum and maximum velocities in z-direction ($u_{z, \min}$, $u_{z, \max}$) and x-direction ($u_{x, \min}$, $u_{x, \max}$) per revolution, are shown for different aspect ratios ($1/\varepsilon$), domain sizes ($L_{x,y,z}$), and initial particle distances (dist).

$1/\varepsilon$	10	12	12	14	12
$L_{x,y,z} [\text{dx}]$	576	576	576	576	768
$\text{dist} [\text{dx}]$	16.0	14.8	16.0	16.0	16.0
$D^* [10^{-3} \text{ m}]$	5.72	5.63	5.63	5.92	5.71
$T^* [\text{s}]$	4.35	3.82	3.86	3.75	3.85
$U^* [10^{-3} \text{ m/s}]$	1.31	1.47	1.46	1.58	1.48
$u_{z, \min} [10^{-3} \text{ m/s}]$	1.11	1.20	1.19	1.25	1.23
$u_{z, \max} [10^{-3} \text{ m/s}]$	1.86	2.09	2.07	2.26	2.10
$u_{x, \min} [10^{-6} \text{ m/s}]$	-152	-179	-178	-199	-177
$u_{x, \max} [10^{-6} \text{ m/s}]$	164	196	196	222	196

particles. Moreover, the maximal distance between the particles in x-direction converges to a value that depends on the aspect ratio, but not on the initial separation (see Fig. 10 and Fig. 11). The minimal distance is hardly affected by these parameters.

6.4. Tumbling results for ellipsoids using SBF and comparison to LBM results

The slender body formulation results for two tumbling particles in a periodic domain are presented in Tab. 6 for different domain sizes and particle distances equivalent to the LBM simulations. Similar to the LBM results, both

Table 6. Simulation results using the slender body formulation for two tumbling fibers in a periodic domain filled with water. The spherocylinder radius is $r = 4 \text{ dx}$.

$1/\varepsilon$	10	12	12	14	12
$L_{x,y,z} [\text{dx}]$	576	576	576	576	768
$\text{dist} [\text{dx}]$	15.0	14.9	15.1	15.1	15.1
$D^* [10^{-3} \text{ m}]$	6.40	6.17	7.20	9.01	5.31
$T^* [\text{s}]$	4.50	3.91	4.53	5.73	3.84
$U^* [10^{-3} \text{ m/s}]$	1.42	1.57	1.53	1.58	1.61
$u_{z, \min} [10^{-3} \text{ m/s}]$	1.23	1.32	1.31	1.35	1.36
$u_{z, \max} [10^{-3} \text{ m/s}]$	2.00	2.36	2.35	2.58	2.40
$u_{x, \min} [10^{-6} \text{ m/s}]$	-180	-224	-224	-260	-224
$u_{x, \max} [10^{-6} \text{ m/s}]$	180	224	224	260	224

u_z and U^* increase with the aspect ratio and with the domain size for constant aspect ratio. However, these velocities are more sensitive to the domain size than for the LBM. Moreover, the initial distance influences U^* stronger than for the LBM, whereas u_z is hardly affected. In contrast to the LBM results, the SBF period time T^* does not systematically depend on the aspect ratio whereas the period distance D^* tends to increase with $1/\varepsilon$. However, D^* depends strongly on both domain size and initial separation distance. With increasing aspect ratio, the velocities u_x increase but are not sensitive to initial distances and domain sizes, like for the LBM.

A comparison of the values presented in Tab. 6 except for T^* and U^* to the corresponding values in Tab. 5 reveals a relative difference of approximately 10 – 20% for $1/\varepsilon = 10, 12$. This difference can be attributed to the different shapes of the particles in the LBM and the SBF respectively, see the discussion in Sec. 5.3. However, for $1/\varepsilon = 14$ the difference is larger, especially for quantities related to the periodicity of the tumbling motion, T^* and D^* . For these quantities the relative difference is now in the order of 35%. In addition to the effect of different particle shape, the combined effect of particle and fluid inertia could play a role here that are both only present in the LBM. Since the velocity of the tumbling particles increases with growing particle lengths, so does the Reynolds

number as well as the importance of fluid inertia. Furthermore, all values obtained with the LBM simulations are consistently lower than the values obtained with the SBF. All of the above is in line with the findings for one sedimenting particle presented in Sec. 5.3.

Another difference between the two methods that also can be attributed to inertial effects only being present in the LBM simulations, is that the SBF results depend strongly on the initial center-to-center distance between the particles, see Fig. 12. For the LBM the situation is different. In

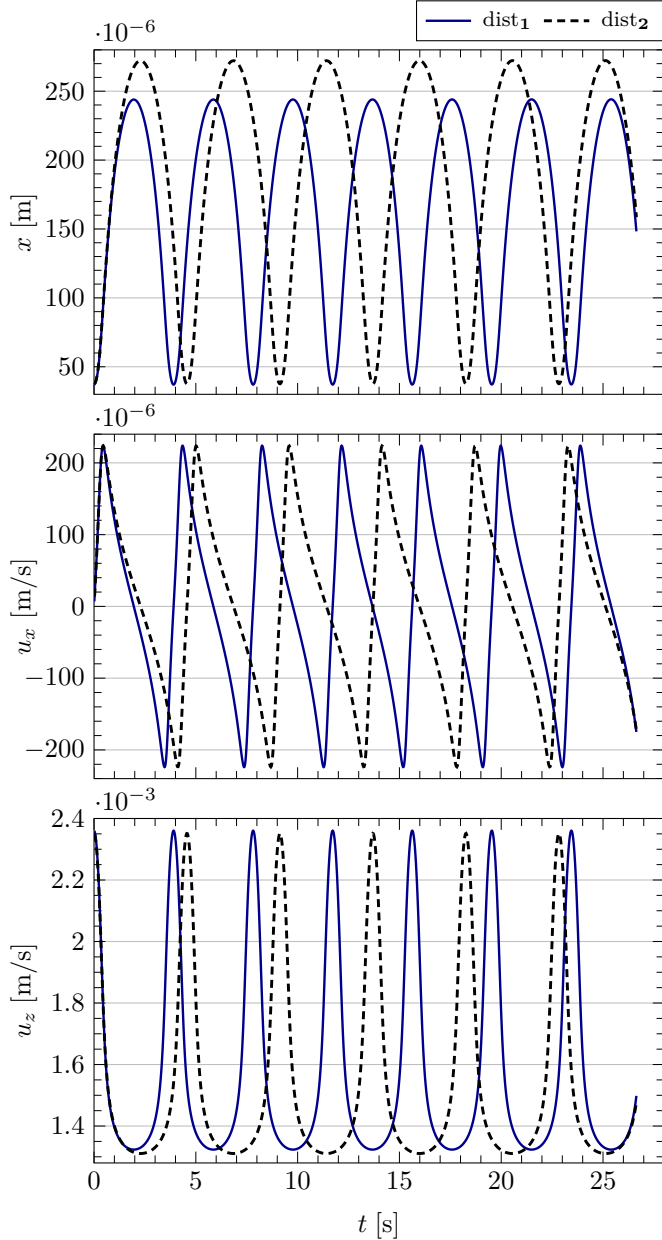


Figure 12. SBF results for tumbling motion of two fibers with radius $r = 4 \text{ dx}$ and aspect ratios $1/\varepsilon = 12$ for initial fiber distances of $\text{dist}_1 = 14.9 \text{ dx}$ and $\text{dist}_2 = 15.1 \text{ dx}$. The size of the periodic domain is $[576 \text{ dx}]^3$.

Fig. 11 we see that the difference caused by starting with two particles at two different center-to-center distances decreases with time, and the curves will eventually coincide. In the SBF, the difference in the resulting curves stay the same throughout the whole simulation.

In the upper diagram of Fig. 13 we show a comparison of the sedimentation velocity for a particle with $1/\varepsilon = 12$ obtained with the LBM and the SBF for initial distances 16 dx and 14.9 dx , respectively. The results agree well on a qualitative level. However, for the SBF the sedimentation velocity is larger and the period time is slightly longer than for the LBM. This is consistent with the results for single particles presented in Sec. 5.3, where the particle velocities of the SBF for ellipsoids are higher than those of the LBM for spherocylinders, due to the different particle shapes.

6.5. Comparison of tumbling orbits from LBM and SBF

The tumbling motion of elongated particles can also be characterized by orbits in phase space, i. e., the space of particle positions and velocities. Since the particle motion is periodic in the direction perpendicular to the sedimentation direction, the orbits in phase space are represented by closed curves. We present the periodic orbits for LBM and SBF simulations.

The tumbling orbits obtained from the LBM simulations are shown in the middle diagram of Fig. 13 for spherocylinders in a periodic, cubic domain. As shown in Fig. 10, the LBM simulations converge towards periodic motion in x-direction after a few revolutions, i. e., the orbits are asymptotically periodic. This effect can be attributed to the inertia considered by the LBM. For the aspect ratio $1/\varepsilon = 10$, the convergence takes the longest, with increasingly larger cycles in x-direction. The reason for this convergence behavior is that the initial separation distance for $1/\varepsilon = 10$ differs the most from the preferred distance (see Fig. 10). The next longer particles with $1/\varepsilon = 12$ converge faster, and the maximal separation in x-direction gets larger at first, too. For $1/\varepsilon = 14$, the maximal particle separation at the first revolution is the highest but converges quickly. Both, terminal maximal separation and velocity magnitude, increase with particle length. However, minimal positions and maximal velocity magnitudes in x-direction do not change with the revolutions. Moreover, the orbits are not symmetric w.r.t. the ordinate because the maximal separation velocity is higher than the maximal approach velocity.

The periodic orbits obtained from the SBF simulations are shown in the lower diagram in Fig. 13. These orbits exhibit in principle the same behavior as the LBM results. The shape of the curves is similar, and the maximal separation distance increases with the particle length. However, the initial minimum separation distance is retained and thus differs for the aspect ratio $1/\varepsilon = 10$ from the longer particles. Moreover, the terminal periodic orbit is already

obtained after the first revolution as there is no inertia, and the maximal separation and approach velocities have the same magnitude for a given particle length.

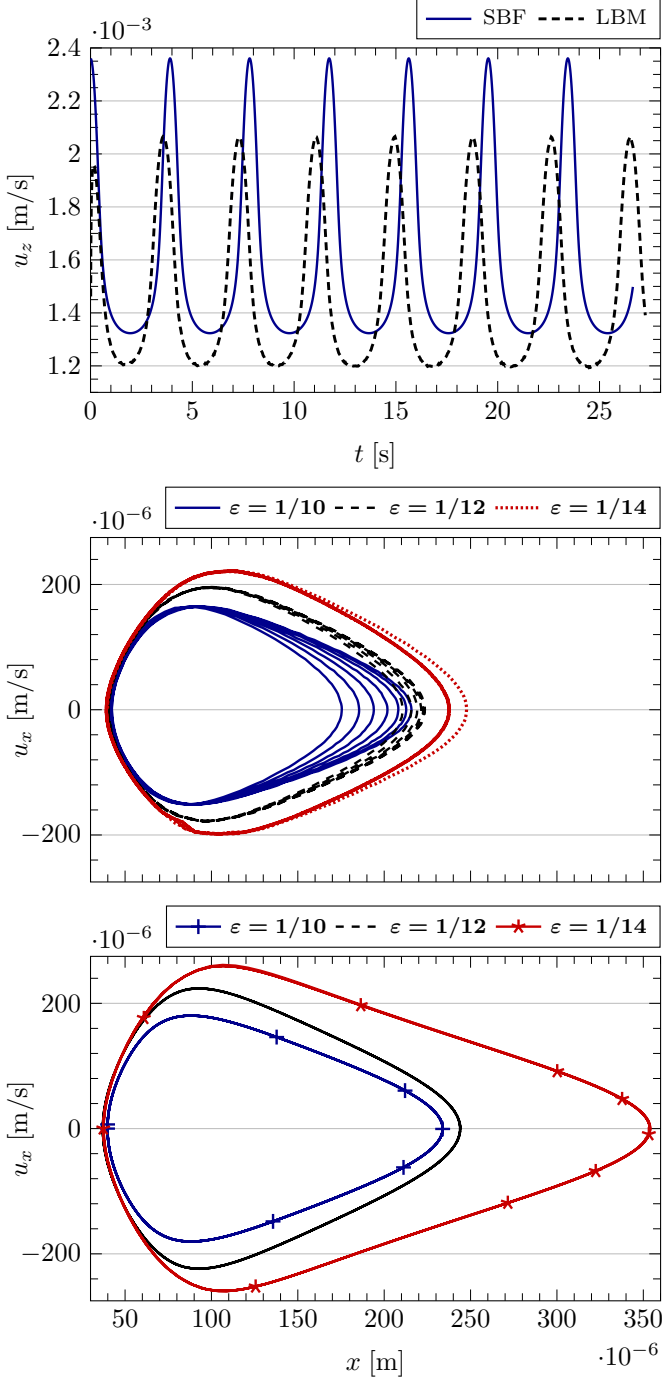


Figure 13. Comparison of the results from LBM and SBF for tumbling motion of two particles with radius $r = 4 \text{ dx}$ and different aspect ratios $1/\epsilon$ and initial distance 16 dx in a periodic domain of size $[576 \text{ dx}]^3$. The upper diagram shows the particle velocity in z -direction over time for $1/\epsilon = 12$. The middle and lower diagrams show the tumbling orbits in phase-space (x -position vs. x -velocity) for LBM and SBF, respectively.

7. Conclusions

In this article, we have validated and compared different methods for elongated particles in creeping flows. The SBF models hydrodynamic interactions of elongated ellipsoidal particles in flow based on an asymptotic formulation in the slenderness parameter. Hence the model accuracy increases with aspect ratio. The LBM simulates hydrodynamic interactions by an explicit computation of the flow field and models the momentum exchange between fluid and particles. Here, the flow is represented on a lattice, and the particles are modeled as spherocylinders.

To validate the LBM simulations, LBM and SBF results for the translational and rotational motion of single elongated particles were compared to analytical solutions for cylinders according to the theories of Cox [27] and Tirado et al. [28]. While the different theories for cylinders and the results for spherocylinders converge quickly with increasing aspect ratio $1/\epsilon$, the SBF solutions for ellipsoids approach these results only for extremely high aspect ratios. The particle shape is identified as the dominant factor for the different velocities of (sphero-)cylinders and ellipsoids. This shape effect explains the consistently lower velocities for the LBM than for the SBF that deviate by about 10% to 16% for translation and by about 12% to 13% for rotation at $1/\epsilon \geq 8$. Overall, the terminal velocities of the different theories converge faster for sidewise orientation w.r.t. the applied force than for lengthwise orientation. The translational velocities for spherocylinders agree very well with the theory of Tirado et al. for cylinders of full spherocylinder lengths, apart from retarding wall effects in the LBM simulations at high aspect ratios. For rotational motion, the angular velocities of spherocylinders are slightly higher than predicted by Tirado et al. for cylinders of full spherocylinder length. We find that in the LBM simulations of single particles, inertial effects play only a minor role compared to shape and wall effects. Finally, the flow field around sidewise and lengthwise moving spherocylinders obtained from LBM simulations is compared. The comparison shows that for sidewise motion the fluid is affected at higher distances, leading to lower sedimentation velocities. Moreover, the counterflux of fluid in the closed domain becomes visible that results in the retarding wall effect.

After the single particle motion validation, the tumbling motion of two elongated particles was examined in a periodic domain. For the LBM simulations, the flow field around the tumbling particles was visualized. The particle trajectories obtained from both, LBM and SBF simulations, were compared in diagrams, including a representation of the tumbling orbits in phase-space. The qualitative agreement of the LBM and SBF simulation results is good, whereas quantitative differences become apparent. Consistent with the single particle motion, the characteristic tumbling parameters differ by about 10 – 20% for aspect ratios of $1/\epsilon = 10, 12$. For an aspect ratio of 14 the dif-

ferences increase, which might partially be attributed to higher differences in the velocities of single lengthwise sedimenting particles.

In contrast to the SBF, a preferred maximal particle separation distance exists for the LBM in the direction perpendicular to gravity, which depends on the aspect ratio and can be attributed to inertia. This effect is similar to the drift to stable orbits due to inertia examined in Mao & Alexeev [25] for the motion of spheroidal particles in shear flow. Moreover, Jung et al. [5] report that the experimental tumbling results for rods are insensitive to the initial separation and converge to the preferred distance. Also the increasing mean sedimentation velocities with particle length observed in the LBM and SBF simulations agree with the experimental investigations in [5].

The strengths of the SBF compared to the LBM lie in its significantly lower computational effort as well as in its ability to simulate zero Reynolds number flows. However, the SBF relies on high aspect ratios to accurately model elongated particles, and other boundary conditions than periodic or free space are not as straight forward as in the LBM. The LBM can in contrast simulate complex geometries and nearly arbitrary particle shapes, only restricted by the pe in this respect. Moreover, the LBM is able to consider inertia, which allows physically more realistic simulations and a better comparison to experiments. The high parallel efficiency of the LBM allows its execution on massively parallel clusters and compensates for its higher computational effort.

A possible extension of the SBF is the implementation of wall boundary conditions. Wall treatments in a boundary integral setting have been found to be challenging, and the literature is sparse. The most straightforward way to include these outer boundaries is to treat the wall in the same way as the immersed objects. A boundary integral over the wall is incorporated in the formulation and is discretized using special quadrature. This approach yields extra unknowns that must be computed and thus increases computational cost. The number of additional unknowns will depend on the size of the domain as well as on the resolution. A different way of including wall boundary conditions in the SBF is to use the method of images[50]. However, this method is only feasible for one or two parallel plane boundaries.

In the future we may compare the two examined methods for elongated particles in flows subject to wall boundary conditions and simulate the interactions of many sedimenting particles, including LBM simulations at higher Reynolds number. The LBM may also be applied to simulate collisions of elongated particles with walls and their motion in complex geometries. Further work could include multiphysics simulations of charged elongated particles in fluids subject to electric fields and their deposition on a charged surface, similar to the simulations with spheres in [20].

Appendix A. Detailed LBM results for single particle motion

Additional details on LBM results from Sec. 5.

Table A.7. LBM sedimentation velocities U_{LBM}^* of spherocylinders with different aspect ratios $1/\varepsilon$ and radius $r = 4 \text{ dx}$ ($\text{dx} = 10^{-5} \text{ m}$), in $[2560 \text{ dx}]^2 \times 2688 \text{ dx}$ domain with free-slip boundaries, and angular velocities ω_{LBM}^* in $[816 \text{ dx}]^3$ domain with no-slip boundaries. Fluctuations due to obstacle mappings $\delta_U = (U_{\text{max}}^* - U_{\text{min}}^*)/U_{\text{LBM}}^*$ and δ_ω (defined analogously) are shown, together with Reynolds numbers based on U_{LBM}^* and diameter ($\text{Re}_{p,d}$) or length ($\text{Re}_{p,L}$), or tip velocity ($\text{Re}_{\text{tip},d}$, $\text{Re}_{\text{tip},L}$). LBM velocities for lengthwise/sidewise translational- and rotational motion are compared to analytical solutions by Tirado et al. [28] for cylinders with lengths including (indicated by ‘Tir,wC’) and excluding (‘Tir,nC’) spherocylinder end-caps. Differences between LBM and Tirado solutions are shown as relative deviations $\Delta_r U$ and $\Delta_r \omega$ w.r.t. the Tirado solutions.

$1/\varepsilon$		4	6	8	10	12	14
L [10^{-3} m]		0.16	0.24	0.32	0.40	0.48	0.56
l e n g t h w	U_{LBM}^* [10^{-6} m/s]	503	419	363	324	294	269
	δ_U [%]	0.80	0.47	0.15	0.40	0.35	0.30
	$\text{Re}_{p,d}$	0.040	0.034	0.029	0.026	0.023	0.022
	$\text{Re}_{p,L}$	0.080	0.10	0.12	0.13	0.14	0.15
	$U_{\text{Tir,nC}}$ [10^{-6} m/s]	653	481	409	361	325	297
	$\Delta_r U$ [%]	-22.9	-12.9	-11.2	-10.2	-9.7	-9.3
	$U_{\text{Tir,wC}}$ [10^{-6} m/s]	481	409	361	325	297	273
	$\Delta_r U$ [%]	4.59	2.38	0.65	-0.28	-1.05	-1.58
	U_{LBM}^* [10^{-6} m/s]	447	349	291	252	223	201
	δ_U [%]	0.78	0.80	0.79	0.87	0.83	0.81
s i d e w i s e	$\text{Re}_{p,d}$	0.036	0.028	0.023	0.020	0.018	0.016
	$\text{Re}_{p,L}$	0.07	0.08	0.09	0.10	0.11	0.11
	$U_{\text{Tir,nC}}$ [10^{-6} m/s]	641	429	344	292	255	227
	$\Delta_r U$ [%]	-30.3	-18.6	-15.4	-13.6	-12.5	-11.6
	$U_{\text{Tir,wC}}$ [10^{-6} m/s]	429	344	292	255	227	205
	$\Delta_r U$ [%]	4.06	1.44	-0.04	-1.06	-1.77	-2.27
	ω_{LBM}^* [$1/\text{s}$]	1.97	1.18	0.829	0.638	0.519	0.436
	δ_ω [%]	8.16	4.78	5.12	4.02	3.17	2.77
	$\text{Re}_{\text{tip},d}$	0.013	0.011	0.011	0.010	0.010	0.010
	$\text{Re}_{\text{tip},L}$	0.025	0.034	0.042	0.051	0.060	0.068
t r a n s l a t i o n	$\omega_{\text{Tir,nC}}$ [$1/\text{s}$]	4.69	1.99	1.25	0.897	0.692	0.561
	$\Delta_r \omega$ [%]	-57.9	-40.7	-33.8	-28.8	-25.0	-22.2
	$\omega_{\text{Tir,wC}}$ [$1/\text{s}$]	1.36	0.909	0.682	0.545	0.455	0.390
	$\Delta_r \omega$ [%]	44.8	29.7	21.6	17.0	14.1	12.0

Acknowledgements

The authors would like to thank Gaby Fleig for support in the correction process. The first author is grateful to the RRZE and LRZ for providing the computational resources on LiMa and SuperMUC, respectively. The second author would like to thank the Deutsche Forschungsgemeinschaft (DFG) for partially funding this project through the Cluster of Excellence ‘Engineering of Advanced Materials’ in Erlangen. The fourth author gratefully acknowledges support by the Institute of Mathematical Sciences at the National University of Singapore, where part of this work was performed.

References

- [1] C. Pozrikidis, Boundary Integral and Singularity Methods for Linearized Viscous Flow, Cambridge University Press, 1992. doi:10.1017/CB09780511624124.
- [2] R. E. Johnson, An improved slender-body theory for Stokes flow, *J. Fluid Mech.* 99 (4) (1980) 411–431. doi:10.1017/S0022112080000687.
- [3] A.-K. Tornberg, K. Gustavsson, A numerical method for simulations of rigid fiber suspensions, *J. Comput. Phys.* 215 (2006) 172–196. doi:10.1063/1.3273091.
- [4] J. Götz, K. Iglberger, M. Stürmer, U. Rüde, Direct Numerical Simulation of Particulate Flows on 294912 Processor Cores, in: Proc. 2010 ACM/IEEE Proc. Int. Conf. for High Performance Computing, Networking, Storage and Analysis, SC '10, IEEE, 2010, pp. 1–11. doi:10.1109/SC.2010.20.
- [5] S. Jung, S. E. Spagnolie, K. Parikh, M. Shelley, A.-K. Tornberg, Periodic sedimentation in a Stokesian fluid, *Phys. Rev. E* 74 (2006) 035302. doi:10.1103/PhysRevE.74.035302.
- [6] G. K. Batchelor, Slender-body theory for particles of arbitrary cross-section in Stokes flow, *J. Fluid Mech.* 44 (1970) 419–440. doi:10.1017/S002211207000191X.
- [7] K. Gustavsson, A.-K. Tornberg, Gravity induced sedimentation of slender fibers, *Phys. Fluids* 21 (12). doi:10.1063/1.3273091.
- [8] D. Saintillan, E. Darve, E. S. G. Shaqfeh, A smooth particle-mesh Ewald algorithm for Stokes suspension simulations: The sedimentation of fibers, *Phys. Fluids* 17. doi:10.1063/1.1862262.
- [9] R. Glowinski, T.-W. Pan, T. Hesla, D. Joseph, A distributed Lagrange multiplier/fictitious domain method for particulate flows, *Int. J. Multiphase Flow* 25 (5) (1999) 755–794. doi:10.1016/S0301-9322(98)00048-2.
- [10] R. Prignitz, E. Bänsch, Particulate flows with the subspace projection method, *J. Comput. Phys.* 260 (2014) 249–272. doi:10.1016/j.jcp.2013.12.030.
- [11] S. Xu, Z. J. Wang, An immersed interface method for simulating the interaction of a fluid with moving boundaries, *J. Comput. Phys.* 216 (2) (2006) 454–493. doi:10.1016/j.jcp.2005.12.016.
- [12] A. J. C. Ladd, Numerical simulations of particulate suspensions via a discretized Boltzmann equation. Part 1. Theoretical foundation, *Journal of Fluid Mechanics* 271 (1994) 285–309. doi:10.1017/S0022112094001771.
- [13] N. Q. Nguyen, A. J. C. Ladd, Lubrication corrections for lattice-Boltzmann simulations of particle suspensions, *Phys. Rev. E* 66 (4) (2002) 046708. doi:10.1103/PhysRevE.66.046708.
- [14] S. Bogner, S. Mohanty, U. Rüde, Drag correlation for dilute and moderately dense fluid-particle systems using the lattice boltzmann method, *Int. J. Multiphase Flow* 68 (0) (2015) 71–79. doi:10.1016/j.ijmultiphaseflow.2014.10.001.
- [15] C. Feichtinger, S. Donath, H. Köstler, J. Götz, U. Rüde, WaL-Berla: HPC software design for computational engineering simulations, *J. Comput. Sci.* 2 (2) (2011) 105–112. doi:10.1016/j.jocs.2011.01.004.
- [16] K. Iglberger, Software design of a massively parallel rigid body framework, Ph.D. thesis, University of Erlangen-Nürnberg (2010).
- [17] K. Iglberger, U. Rüde, Massively Parallel Rigid Body Dynamics Simulation, *CSR* 23 (3–4) (2009) 159–167. doi:10.1007/s00450-009-0066-8.
- [18] C. Godenschwager, F. Schornbaum, M. Bauer, H. Köstler, U. Rüde, A Framework for Hybrid Parallel Flow Simulations with a Trillion Cells in Complex Geometries, in: Proc. Int. Conf. on High Performance Computing, Networking, Storage and Analysis, SC '13, ACM, New York, NY, USA, 2013, pp. 35:1–35:12. doi:10.1145/2503210.2503273.
- [19] E. Fischermeier, D. Bartuschat, T. Preclik, M. Marechal, K. Mecke, Simulation of a hard-spherocylinder liquid crystal with the pe, *Comput. Phys. Commun.* 185 (12) (2014) 3156–3161. doi:10.1016/j.cpc.2014.08.014.
- [20] D. Bartuschat, U. Rüde, Parallel Multiphysics Simulations of Charged Particles in Microfluidic Flows, *J. Comput. Sci.* 8 (0) (2015) 1–19. doi:10.1016/j.jocs.2015.02.006.
- [21] Z.-H. Xia, K. W. Connington, S. Rapaka, P. Yue, J. J. Feng, S.-Y. Chen, Flow patterns in the sedimentation of an elliptical particle, *J. Fluid Mech.* 625 (2009) 249–272. doi:10.1017/S002211200800552.
- [22] D.-M. Nie, J.-Z. Lin, K. Zhang, Flow Patterns in the Sedimentation of a Capsule-Shaped Particle, *Chinese Physics Letters* 29 (8) (2012) 84703. doi:10.1088/0256-307X/29/8/084703.
- [23] L. Jianzhong, S. Xing, Y. Zhenjiang, Effects of the aspect ratio on the sedimentation of a fiber in Newtonian fluids, *J. Aerosol Sci.* 34 (7) (2003) 909–921. doi:10.1016/S0021-8502(03)00039-9.
- [24] X. K. Ku, J. Z. Lin, Inertial effects on the rotational motion of a fibre in simple shear flow between two bounding walls, *Phys. Scripta* 80 (2) (2009) 025801. doi:10.1088/0031-8949/80/02/025801.
- [25] W. Mao, A. Alexeev, Motion of spheroid particles in shear flow with inertia, *J. Fluid Mech.* 749 (2014) 145–166. doi:10.1017/jfm.2014.224.
- [26] M. Doi, S. F. Edwards, The Theory of Polymer Dynamics, Clarendon Press, Oxford, 1986.
- [27] R. G. Cox, The motion of long slender bodies in a viscous fluid. Part 1. General theory, *J. Fluid Mech.* 44 (7) (1970) 791–810. doi:10.1017/S002211207000215X.
- [28] M. M. Tirado, C. L. Martinez, J. G. de la Torre, Comparison of theories for the translational and rotational diffusion coefficients of rod-like macromolecules. Application to short DNA fragments, *J. Chem. Phys.* 81 (4) (1984) 2047–2052. doi:10.1063/1.447827.
- [29] M. M. Tirado, J. G. de La Torre, Translational friction coefficients of rigid, symmetric top macromolecules. Application to circular cylinders, *J. Chem. Phys.* 71 (6) (1979) 2581–2587. doi:10.1063/1.438613.
- [30] M. M. Tirado, J. G. de La Torre, Rotational dynamics of rigid, symmetric top macromolecules. application to circular cylinders, *J. Chem. Phys.* 73 (4) (1980) 1986–1993. doi:10.1063/1.440288.
- [31] R. S. I. Keller, J. B., Slender-body theory for slow viscous flow, *J. Fluid Mech.* 75 (4) (1976) 705–714. doi:10.1017/S0022112076000475.
- [32] T. Götz, Interactions of fibers and flow: Asymptotics, theory and numerics, Ph.D. thesis, Kaiserslautern, Germany (2000).
- [33] F. J. Higuera, S. Succi, R. Benzi, Lattice Gas Dynamics with Enhanced Collisions, *Europhys. Lett.* 9 (4) (1989) 345. doi:10.1209/0295-5075/9/4/008.
- [34] D. d’Humières, Generalized lattice-Boltzmann equations, in: *Rarefied Gas Dynamics: Theory and Simulations*, Vol. 159 of Prog. Astronaut. Aeronaut., 1992, pp. 450–458.
- [35] J. D. Sterling, S. Chen, Stability Analysis of Lattice Boltzmann Methods, *J. Comput. Phys.* 123 (1) (1996) 196–206. doi:10.1006/jcph.1996.0016.
- [36] D. A. Wolf-Gladrow, Lattice-Gas Cellular Automata and Lattice Boltzmann Models: An Introduction, no. 1725 in *Lattice-gas Cellular Automata and Lattice Boltzmann Models: An Introduction*, Springer, 2000.
- [37] X. He, L.-S. Luo, Lattice Boltzmann Model for the Incompressible Navier-Stokes Equation, *J. Stat. Phys.* 88 (3) (1997) 927–944. doi:10.1023/B:J0SS.0000015179.12689.e4.
- [38] Y. H. Qian, D. d’Humières, P. Lallemand, Lattice BGK Models for Navier-Stokes Equation, *Europhys. Lett.* 17 (6) (1992) 479. doi:10.1209/0295-5075/17/6/001.
- [39] I. Ginzburg, J.-P. Carlier, C. Kao, Lattice Boltzmann approach to Richards’ equation, in: *Computational Methods in Water Resources*, Vol. 55 of Developments in Water Science, Elsevier, 2004, pp. 583–595. doi:10.1016/S0167-5648(04)80083-2.
- [40] I. Ginzburg, F. Verhaeghe, D. d’Humières, Two-relaxation-time lattice Boltzmann scheme: About parametrization, velocity, pressure and mixed boundary conditions, *Commun. Comput. Phys.* 3 (2) (2008) 427–478.
- [41] R. Cornubert, D. d’Humières, D. Levermore, A Knudsen layer

- theory for lattice gases, *Physica D: Nonlinear Phenomena* 47 (1–2) (1991) 241–259. doi:10.1016/0167-2789(91)90295-K.
- [42] I. Ginzburg, F. Verhaeghe, D. d’Humières, Study of simple hydrodynamic solutions with the two-relaxation-times lattice Boltzmann scheme, *Commun. Comput. Phys.* 3 (3) (2008) 519–581.
- [43] A. J. C. Ladd, Numerical simulations of particulate suspensions via a discretized Boltzmann equation. Part 2. Numerical results, *Journal of Fluid Mechanics* 271 (1994) 311–339. doi:10.1017/S0022112094001783.
- [44] C. K. Aidun, Y. Lu, E.-J. Ding, Direct analysis of particulate suspensions with inertia using the discrete Boltzmann equation, *Journal of Fluid Mechanics* 373 (1) (1998) 287–311. doi:10.1017/S0022112098002493.
- [45] J. Götz, K. Iglberger, C. Feichtinger, S. Donath, U. Rüde, Coupling multibody dynamics and computational fluid dynamics on 8192 processor cores, *Parallel Comput.* 36 (2) (2010) 142–141. doi:10.1016/j.parco.2010.01.005.
- [46] C. Feichtinger, Design and Performance Evaluation of a Software Framework for Multi-Physics Simulations on Heterogeneous Supercomputers, Ph.D. thesis, University of Erlangen-Nürnberg (2012).
- [47] S. Donath, J. Götz, S. Bergler, C. Feichtinger, K. Iglberger, U. Rüde, waLBerla: The Need for Large-Scale Super Computers, in: *High Performance Computing in Science and Engineering. Garching/Munich 2007*, Springer, 2008, pp. 459–473. doi:10.1007/978-3-540-69182-2_37.
- [48] D. M. Kaufman, T. Edmunds, D. K. Pai, Fast frictional dynamics for rigid bodies, *ACM Trans. Graph.* 24 (3) (2005) 946–956. doi:10.1145/1073204.1073295.
- [49] T. Preclik, U. Rüde, Ultrascale Simulations of Non-smooth Granular Dynamics, arXiv preprint [arXiv:1501.05810](https://arxiv.org/abs/1501.05810).
- [50] J. R. Blake, A note on the image system for a Stokeslet in a no-slip boundary, *Proc. Camb. Philos. Soc.* 70 (1971) 303–310. doi:10.1017/S0305004100049902.